

Transient Corotating Clumps Around Adolescent Low-Mass Stars: Four Years of Complex Rotators from TESS

LUKE G. BOUMA,^{1,*} RAHUL JAYARAMAN,² SAUL RAPPAPORT,² LUISA M. REBULL,¹ ALEXANDRE DAVID-URAZ,^{3,4}
LYNNE A. HILLENBRAND,¹ JOSHUA N. WINN,⁵ GÁSPÁR Á. BAKOS,⁵
—SUGGESTED CONTRIBUTORS, PENDING DISCUSSION, COMMENTS, ANALYSES, ETC—,⁶
MAXIMILIAN N. GÜNTHER,⁶ AND GEORGE R. RICKER²

¹Department of Astronomy, MC 249-17, California Institute of Technology, Pasadena, CA 91125, USA

²MIT Kavli Institute and Department of Physics, 77 Massachusetts Avenue, Cambridge, MA 02139

³Department of Physics and Astronomy, Howard University, Washington DC, 20059

⁴Center for Research and Exploration in Space Science and Technology, and X-ray Astrophysics Laboratory, NASA/GSFC, Greenbelt, MD 20771, USA

⁵Department of Astrophysical Sciences, Princeton University, 4 Ivy Lane, Princeton, NJ 08540, USA

⁶European Space Agency (ESA), European Space Research and Technology Centre (ESTEC), Keplerlaan 1, 2201 AZ Noordwijk, Netherlands

(Received —; Revised —; Accepted —)

ABSTRACT

Complex rotators (CRs) are low-mass pre-main-sequence stars with light curves characterized by periods of 0.2–2 days, amplitudes of a few percent, and slowly-evolving sharp features. The sharp features might be caused by eclipsing clumps of dust or gas orbiting at the corotation radius. To improve our understanding of these enigmatic stars, we conducted a survey for CRs using TESS short-cadence data collected between 2018 July and 2022 September. Our search of 65,760 K and M dwarfs with $T < 16$ and $d < 150$ pc yielded 50 high-quality CRs, most of which are new discoveries. Our sample includes the brightest ($T \approx 9.5$), closest ($d \approx 20$ pc), and oldest (≈ 200 Myr) known CRs. One of the new discoveries, LP 12-502, stands out for the complexity of its light curve — with as many as eight flux dips per cycle — and the detail with which the evolution in each dip’s amplitude and phase can be tracked over 1,500 cycles. We argue that corotating gas or dust remains the most viable explanation for CRs. The gas or dust is probably entrained by the star’s magnetic field, and the sharp features may result from a multipolar field topology, a hypothesis supported by correspondences between the light curves of CRs and of two B stars known to have strong multipolar magnetic fields.

Keywords: Weak-line T Tauri stars (1795), Periodic variable stars (1213), Circumstellar matter (241), Star clusters (1567), Stellar magnetic fields (1610), Stellar rotation (1629)

1. INTRODUCTION

All young stars vary in optical brightness, and the origin of such variability is, in most cases, understood. Well-explored sources of optical variability include inhomogeneities on stellar surfaces such as starspots and faculae (e.g. Basri 2021), occultations by circumstellar disks (e.g. Bodman et al. 2017), and, in geometrically favorable circumstances, eclipses by stars and planets (e.g. Rizzuto et al. 2020). More exotic sources of optical variability that are potentially relevant to this work include transiting exocomets (e.g. β Pic; Zieba et al. 2019), disintegrating rocky bodies (e.g. KOI-2700; Rappaport et al. 2014), and occultations by circumstellar plasma clumps (e.g. σ Ori E; Townsend et al. 2005; Townsend & Owocki 2005).

Corresponding author: Luke G. Bouma
luke@astro.caltech.edu

* 51 Pegasi b Fellow

Data from K2 (Howell et al. 2014) and TESS (Ricker et al. 2015) have revealed a new class of variable star for which the root cause of variability is only beginning to become clear: complex rotators (CRs). These objects are identified from their optical light curves, which show nearly periodic troughs that are either sharp or broad; these troughs are often superposed on quasi-sinusoidal spot-like modulation (Stauffer et al. 2017, 2018; Zhan et al. 2019). Some CRs show up to eight dips per cycle. Most CRs are pre-main-sequence M dwarfs with ages of $\approx 5\text{--}150$ million years (Myr), and rotation periods of 0.2–2 days. They are observed to comprise $\approx 1\text{--}3\%$ of M dwarfs younger than 100 Myr (Rebull et al. 2016; Günther et al. 2022). They generally do not show near-infrared excesses indicative of dusty disks, but the wavelength-dependent dip amplitudes of some CRs is consistent with reddening by dust (Onitsuka et al. 2017; Bouma et al. 2020; Günther et al. 2022; Koen 2023). The dip amplitudes and phases usually evolve gradually over tens to hundreds of cycles, although they have occasionally been ob-

served to change abruptly within one cycle (e.g. Stauffer et al. 2017; Palumbo et al. 2022; Popinchalk et al. 2023).

The sharp features of CR light curves can have durations as short as 5% of the rotation period (P_{rot}), which is too short to be caused by starspots rotating into and out of view. Starspots produce flux variations with characteristic timescales of P_{rot} and $0.5P_{\text{rot}}$. With finely-tuned viewing geometries, starspots can produce dip durations as short as $\approx 0.2P_{\text{rot}}$, but in such cases, limb darkening causes the dip amplitudes to be smaller than the observed amplitudes of $\sim 1\%$ (see Stauffer et al. 2017, Figures 37-41). Thus, a “starspot-only” scenario can be ruled out for many CRs (Stauffer et al. 2017; Zhan et al. 2019; Koen 2021). Given that many CRs cannot be explained by starspots alone, and working under the assumption that all CRs share the same basic physical scenario, we discard the “starspot-only” scenario. Instead, the correct explanation probably involves material above the stellar surface that is spatially confined with sharp boundaries (e.g. Stauffer et al. 2017; Günther et al. 2022).

Figure 1 illustrates two proposed models for the extrinsic material. The first scenario invokes opaque dust “clumps” that orbit near the Keplerian corotation radius [$R_c = (GM/\Omega^2)^{1/3}$, where $\Omega = 2\pi/P_{\text{rot}}$] and periodically transit the star (Stauffer et al. 2017; Sanderson et al. 2023). The second scenario invokes “prominences”, long-lived condensations of cool, dense, marginally-ionized gas that are embedded within the hotter corona and corotate with the star (Collier Cameron & Robinson 1989; Jardine & Collier Cameron 2019; Waugh & Jardine 2022). These hypothetical structures are analogous to quiescent prominences and filaments seen in the solar corona (see e.g. Vial & Engvold 2015), though rather than existing at a fraction of the stellar radius as in the solar case, they would exist at distances of a few stellar radii. A final possibility is that a thin optically-thick ring obscures a small portion of the stellar photosphere (Zhan et al. 2019). Hot spots passing behind such a ring could produce sudden dips. We do not favor this scenario due to two issues discussed in Appendix A.

The dust clump and prominence hypotheses are qualitatively similar, except that one invokes opacity from dust, while the other invokes opacity from gas, likely bound-free transitions in hydrogen or perhaps a molecular opacity. However unambiguous evidence in support of any particular scenario has yet to be acquired. Such evidence might include a spectroscopic detection of silicate $10\,\mu\text{m}$ dust absorption during a dip, or perhaps detection of transient Balmer-line excesses as a function of cycle phase, similar to observations made in systems such as AB Dor (see Collier Cameron 1999) or PTFO 8-8695 (Johns-Krull et al. 2016).

CRs remain mysterious because they have been both hard to discover and hard to characterize. They are hard to discover because they are rare: CRs comprise $\approx 1\%$ of the youngest $\approx 1\%$ of M dwarfs (Rebull et al. 2018). Out of the millions of stars monitored by K2 and TESS, about 50 CRs have been reported to date (Rebull et al. 2016; Stauffer et al. 2017, 2018; Zhan et al. 2019; Bouma et al. 2020; Günther et al. 2022; Popinchalk et al. 2023). They have been hard to

characterize because many of the known CRs are relatively faint; the initial K2 discoveries (Rebull et al. 2016; Stauffer et al. 2017) were M2-M6 dwarfs at distances $\gtrsim 100\,\text{pc}$, yielding optical brightnesses of $V \approx 15.5$ to $V > 20$. At such magnitudes, high-resolution time-series spectroscopy is out of reach with current facilities, despite the potential utility of such observations.

In this work, we aim to find bright and nearby CRs, since these objects will be the most amenable to detailed photometric and spectroscopic analyses. To do this, we use 120-second cadence data acquired by TESS between 2018 July and 2022 September (Sectors 1-55; Cycles 1-4). We present our search methods in Section 2, and the resulting CR catalog in Section 3. The observed evolution of many CRs over a two-year baseline is described in Section 4, including a deep-dive into the behavior of an especially interesting object, LP 12-502. We discuss a few implications in Section 5, and conclude in Section 6.

Some comments on nomenclature are needed. What we are calling “complex rotators” (Zhan et al. 2019; Günther et al. 2022; Popinchalk et al. 2023) have also been called “transient flux dips”, “persistent flux dips”, and “scallop shells” by Stauffer et al. (2017), or more generally “complex periodic variables” by Koen (2023). The CRs should not be conflated with “dippers”, which are classical T Tauri stars with infrared excesses, and which show large-amplitude variability linked to obscuring inner disk structures and accretion hot spots (Cody et al. 2014; Robinson et al. 2021). The phenomenology and stellar properties of CRs and dippers are quite different (though see Sections 3.3 and 5.7). While we considered other possibilities, we ultimately concluded that “complex rotator” correctly draws attention to the fact that rotation will play a fundamental role in explaining these objects, and that their key defining feature is the complexity of their optical light curves relative to the quasi-sinusoidal modulations of starspots.

2. METHODS

2.1. Stellar selection function

To construct our sample, we analyzed the short-cadence data acquired by TESS between 2018 July 25 and 2022 September 1 (Sectors 1-55). Specifically, we used the 120-second cadence light curves produced by the Science Processing and Operations Center at the NASA Ames Research Center (Jenkins et al. 2016). While the TESS data products from these sectors also included full frame images with cadences of 600 and 1800 seconds for a larger number of sources, we restricted our attention to the 120-second data for the sake of uniformity and simplicity in data handling. In exchange, we sacrificed both completeness and homogeneity of the selection function. While TESS cumulatively observed $\approx 90\%$ of the sky for at least one lunar month between 2018 July and 2022 September, the 120-second cadence data were collected for only a subset of observable stars that were preferentially nearby and bright (see Fausnaugh et al. 2021). The total 120-second data volume from Sectors 1-55 included

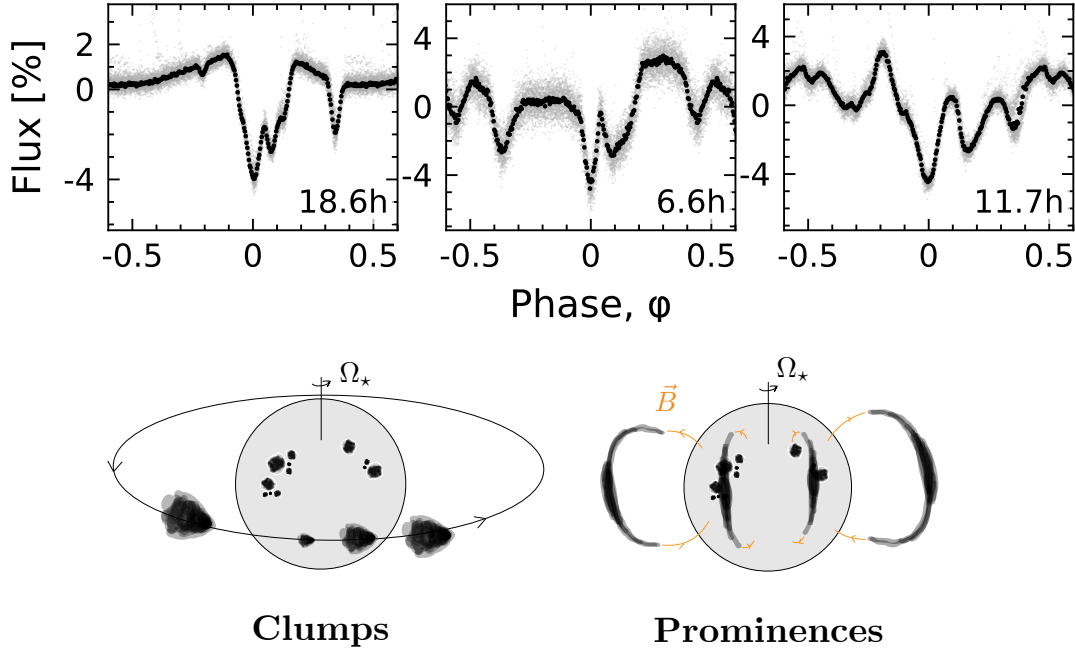


Figure 1. Complex rotators (CRs): *Top:* Phase-folded TESS light curves of three CRs. Each panel shows the average of the data accumulated over one month. Gray circles are raw 2-minute data; black circles are binned to 300 points per cycle. The period in hours is printed in the bottom right corner. Left-to-right, the objects are LP 12-502 (TIC 402980664; Sector 19), TIC 94088626 (Sector 10), and TIC 425933644 (Sector 28). *Bottom:* Cartoon explanations for the phenomenon. The dust clump scenario (left) and prominence scenario (right) both invoke magnetically-entrained corotating material.

1,087,475 short-cadence light curves, which were available for 428,121 unique stars.

To further simplify our search, we defined our target sample as stars with 120-second cadence TESS light curves satisfying the following four conditions:

$$T < 16 \quad (\text{Amenable with TESS}) \quad (1)$$

$$G_{\text{BP}} - G_{\text{RP}} > 1.5 \quad (\text{Red stars only}) \quad (2)$$

$$M_{\text{G}} > 4 \quad (\text{Dwarf stars only}) \quad (3)$$

$$d < 150 \text{ pc} \quad (\text{Close stars only}). \quad (4)$$

Here, $M_{\text{G}} = G + 5 \log(\varpi_{\text{as}}) + 5$ is the Gaia G -band absolute magnitude, ϖ_{as} is the parallax in units of arcseconds, and d is a geometric distance defined by inverting the parallax and ignoring any zero-point correction. We performed this selection by cross-matching TIC8.2 (Stassun et al. 2019; Paegert et al. 2021) against the Gaia DR2 point-source catalog (Gaia Collaboration et al. 2018). We opted for Gaia DR2 rather than DR3 because the base catalog for TIC8 was Gaia DR2, which facilitated a one-to-one crossmatch using the Gaia source identifiers. The target sample ultimately included 65,760 M dwarfs and late-K dwarfs, down to $T < 16$ and out to $d < 150$ pc. For stars with multiple sectors of TESS data available, we searched for CR signals independently. In total, our 65,760 star target list included 180,017 month-long light curves.

We assessed the completeness of our selection function by comparing the number of stars with TESS Sector 1–55 short-

cadence data against the number of Gaia DR2 point sources. We required all stars to meet conditions 1–4. The results are shown in Figure 2. TESS 2-minute data exist for $\approx 50\%$ of $T < 16$ M and late-K dwarfs at ≈ 50 pc. Within 20 pc, $\gtrsim 80\%$ of the $T < 16$ M and late-K dwarfs have at least one sector of short-cadence data. Beyond 100 pc, $\lesssim 10\%$ of such stars have any short-cadence data available. This can be translated into our sensitivity for the lowest mass stars by considering that the spectral type of a $T=16$ star at $d=50$ pc is $\approx \text{M}5.5\text{V}$, corresponding to a main-sequence mass of $\approx 0.12 M_{\odot}$.

2.2. CR discovery

Previous methods for finding CRs have included visually examining stars in young clusters (Rebull et al. 2016; Stauffer et al. 2017) and automatically flagging rapid rotators with a large number of strong Fourier harmonics (Zhan et al. 2019). The latter approach still requires visual vetting, since “stars with strong Fourier harmonics” is a designation that includes objects such as eclipsing binaries or multiple stars blended into a single photometric aperture. In this work, we implemented a new search approach based on counting the number of sharp local minima in phase-folded light curves, while also using the Fourier approach. We applied these two search techniques independently.

2.2.1. Counting dips

The dip counting technique aims to count sharp local minima in phase-folded light curves. CRs will preferably have at

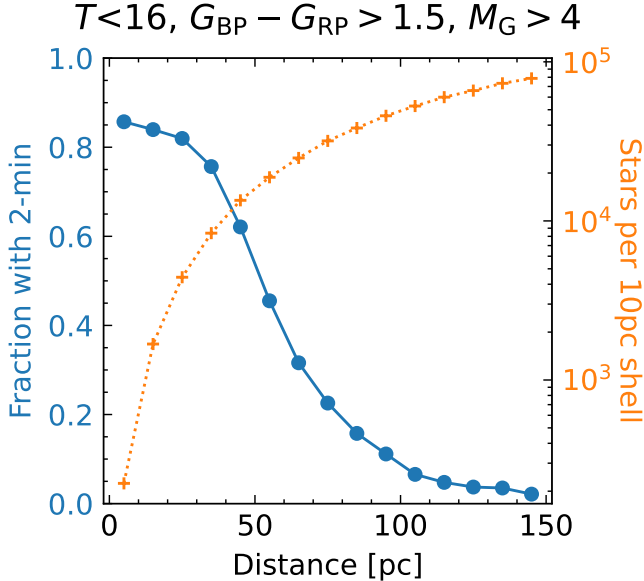


Figure 2. Completeness of the TESS 2-minute cadence data for late-K and early M dwarfs near the Sun, from Sectors 1-55.

The orange dotted curve shows the number of stars in successive radial shells, each with a width of 10 pc. To be counted, these stars must meet the listed conditions: they must be red ($G_{\text{BP}} - G_{\text{RP}} > 1.5$) dwarf stars ($M_G > 4$) amenable for TESS observations ($T < 16$). The blue solid curve shows the fraction of such stars with at least one sector of TESS 2-minute cadence data acquired between Sectors 1-55. The latter data comprise the selection function for our complex rotator search.

least three such minima in order to be distinct from false positives such as synchronized and spotted binaries (“RS CVn” stars).

For our dip-counting pipeline, we began with the PDC_SAP flux for each sector, removed non-zero quality flags, and normalized the light curve to one by dividing out its median value. We then flattened the light curve using a 5-day sliding median filter, as implemented in wotan (Hipke et al. 2019). On the resulting cleaned and flattened light curve, we ran a periodogram search, opting for the Stellingwerf (1978) phase dispersion minimization (PDM) algorithm implemented in astrobase (Bhatti et al. 2021) due to its shape agnosticism. If a period P below 2 days was identified, we reran the periodogram at a finer grid to improve the accuracy of the period determination.

Once a star’s period was identified, we binned the phased light curve to 100 points per cycle. To separate “sharp” local minima from smooth spot-induced variability, we then iteratively fit robust penalized splines to the wrapped phase-folded light curve, excluding points more than two standard deviations away from the local continuum (Hipke et al. 2019). The maximum number of equidistant spline knots per cycle is the parameter in this framework that controlled the meaning of “sharp”—we allowed at most 10 such knots per cycle, though for most stars fewer knots were preferred based

on cross-validation using an ℓ^2 -norm penalty. An example fit is shown in panel (e) of Figure 3.

We then identified local minima in the resulting residual light curve using the SciPy `find_peaks` utility (Virtanen et al. 2020), which is based on comparing adjacent values in an array. For a peak to be flagged as significant, we required it to have a width of at least $0.02P$, and a height of at least twice the point-to-point RMS. This latter quantity is defined as the 68th percentile of the distribution of the residuals from the median value of $\delta f_i \equiv f_i - f_{i+1}$, where f is the flux and i is an index over time.

To identify local minima near the edges of the phased light curve, which usually would cover phases $\phi \in [0, 1]$, we performed the entire procedure over a phase-folded light curve spanning $\phi \in [-1, 2]$, by duplicating and concatenating the ordinary phase-folded light curve. The free parameters we adopted throughout this analysis procedure, for instance the maximum number of spline knots per cycle, and how large and wide of a local minimum to consider a “true dip”, were chosen during testing based on their ability to correctly re-identify a large fraction (>90%) of previously known CRs, while also being able to consistently reject common false positives such as rapidly rotating spot-induced variability and typical eclipsing binaries.

Overall, for a star to proceed to manual examination, we required that it have a peak PDM period below two days, and that it exhibited at least three sharp local minima (as algorithmically reported) in at least one observed TESS sector.

2.2.2. Fourier analysis

We performed an independent search for strongly periodic phenomena using a Fourier-based approach, following Zhan et al. (2019) and Pribulla et al. (2023, their Section 1.3). Starting with the PDC_SAP light curves, we normalized each light curve, and then re-binned it into equal width 120-second bins to account for the uneven spacing in the TESS data, as well as the data gap caused by satellite downlink during each sector. We then padded the data to ensure that the light curve had a length that was a power of two, as described by Zhan et al.. Taking the Fourier transform of the padded light curve using `numpy.fft`, we then searched for peaks with a significance of over 12σ within a set of 500 frequency bins.

If a peak of such significance was found, we generated a “summary sheet” with information about the star, its full and folded light curves, Fourier transform, potential contaminating stars, and information about these contaminating stars. In the sectors for which we performed this analysis, we found that “summary” sheets were generated for $\approx 10\%$ of the 20,000 120-second targets in a given sector. We then manually reviewed each summary sheet, and visually labeled each star based on its morphology (including e.g. eclipsing binary, CR, RS CVn, or cataclysmic variable). CRs that were observed in multiple sectors had their light curves stitched together and analyzed for a more accurate period determination.

2.2.3. Manual vetting

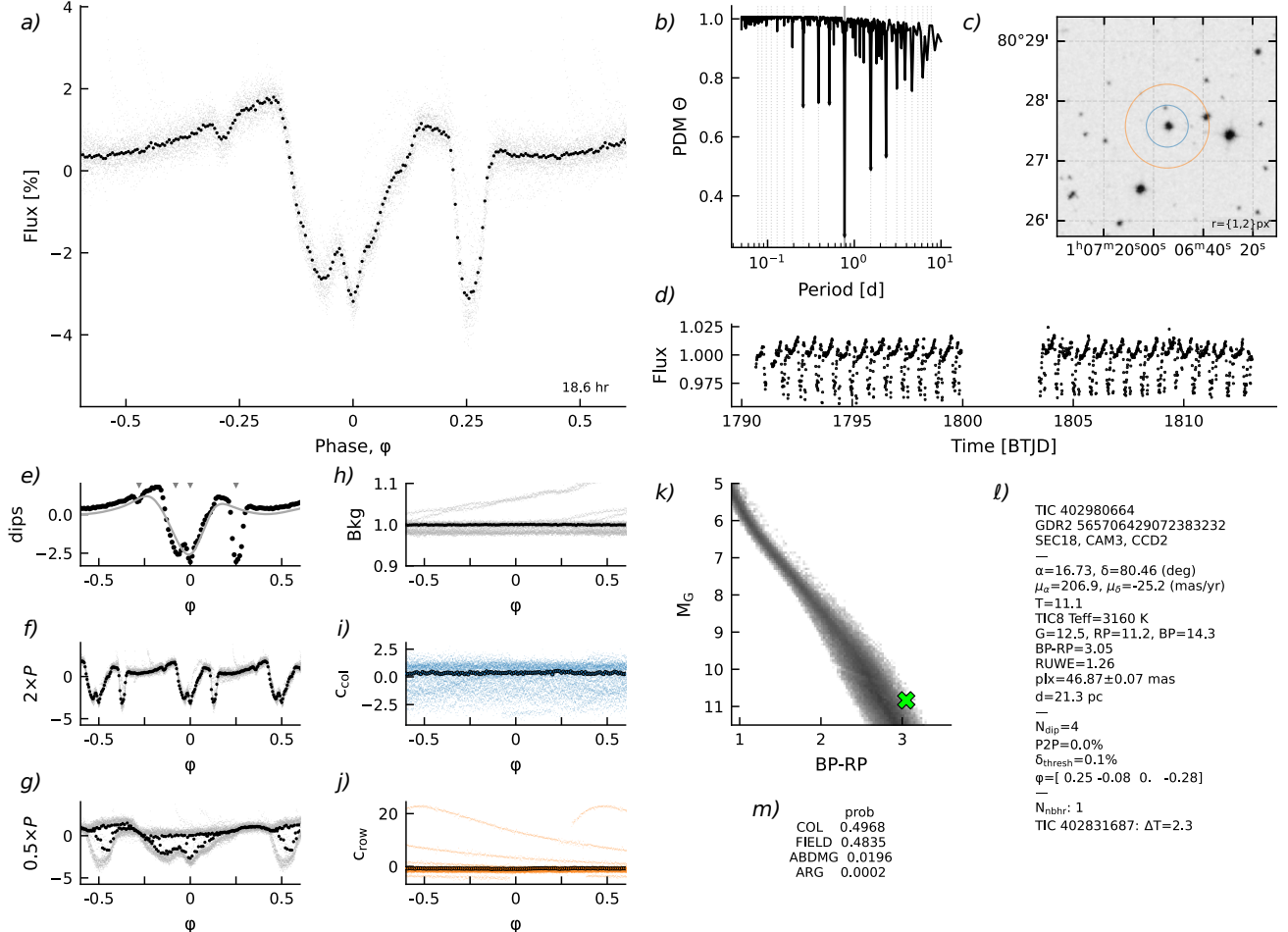


Figure 3. Validation plots used to label CRs. The complete figure set, with one image per sector for each of the 66 objects in Table 1 is available in the online journal. **For internal collaboration review:** <https://www.dropbox.com/sh/khtwk5a6z0zgrif/AABRG21Ire7VS4BUnaD1hOR8a?dl=0>. Panels are as follows. *a*): Phase-folded light curve; gray points are raw 2-minute data and black points are binned to 200 points per cycle. The adopted period is given in the lower-right corner. *b*): Phase-dispersion minimization (PDM) periodogram. Dotted lines show up to the 10th harmonic and subharmonic. *c*): DSS finder chart, with 1- and 2-TESS pixel radius circles displayed for scale. *d*): Cleaned light curve, binned to 20-minute cadence, in Barycentric TESS Julian Date (BTJD). *e*): Phase-folded light curve, binned to 100 points per cycle. The gray line denotes the automated spline-fit to the wrapped phase-folded light curve, and small gray triangles denote automatically identified local minima. *f*): Phase-folded light curve at twice the peak period. *g*): Phase-folded light curve at half the peak period. *h*): Phase-folded time-series within the “background” aperture defined in the SPOC light curves. *i*): Phase-folded flux-weighted centroid in the column direction. *j*): Phase-folded flux-weighted centroid in the row direction. *k*): Gaia DR2 color–absolute magnitude diagram. The gray background denotes stars within 100 pc from [Gaia Collaboration et al. \(2021\)](#). *l*): Information from Gaia DR2, TIC8, and the automated dip-counting search pipeline. “Neighbors”, abbreviated “nbhr”, are listed within apparent distances of 2 TESS pixels if $\Delta T < 2.5$. *m*): BANYAN- Σ v1.2 association probabilities, calculated using positions, proper motions, and the parallax.

We assessed whether the objects found using the dip-counting (Section 2.2.1) and Fourier (Section 2.2.2) techniques were consistent with expectations for CRs by assembling the data shown in Figure 3. We labeled a star as a “good” CR if at least one TESS sector showed what we viewed as the unambiguous signatures of the class (short period; at least three dips or else otherwise oddly-shaped dips; relative stability over a timescale of 30 days). We independently noted stars that we thought could be CRs, but that were more ambiguous.

Broadly speaking, the most common false positive triggers for both the Fourier and dip-counting techniques were eclipsing binaries, spot-induced variability from rapid rotators, and variability from neighboring, off-target stars. Typical false positive rates from our dip-counting pipeline were 5:1, with 368 unique stars flagged, and about 20% being labeled either “good” or “possible” CRs. The Fourier analysis was not amenable to calculating a similar false-positive rate, because it was implemented as a general variability search; its results are also being used for analyses on topics other than CRs.

2.3. Stellar properties

Ages—We estimated the stellar ages by making probabilistic spatial and kinematic associations between the CRs and known clusters in the solar neighborhood. For most stars in our sample, we did this using BANYAN Σ (Gagné et al. 2018).¹ This algorithm calculates the probability that a given star belongs to one of 27 young clusters (or “associations”) within 150 pc of the Sun, by modeling the clusters as multivariate Gaussians in 3-D position and 3-D velocity space. We used the Gaia DR2 sky positions, proper motions, and distances to calculate the membership probabilities. BANYAN Σ in turn analytically marginalizes over the radial velocity dimension. The probabilities returned by this procedure are qualitatively useful, but should be assessed with caution due to the non-Gaussian nature of most groups within the solar neighborhood (see e.g. Kerr et al. 2021, Figure 10).

For a few cases where BANYAN Σ yielded ambiguous results, we consulted the meta-catalog of young, age-dated, and age-dateable stars within from Bouma et al. (2022), and also searched the local volume around each star for co-moving companions.²

Effective temperatures, radii, and masses—We determined the stellar effective temperature and radii by fitting the broadband spectral energy distributions (SEDs); we then estimated the masses by interpolating against the sizes, temperatures, and ages of the PARSEC v1.2S models (Bressan et al. 2012; Chen et al. 2014).

For the SED fitting, we used astroARIADNE (Vines & Jenkins 2022). We adopted the BT-Settl stellar atmosphere models (Allard et al. 2012) assuming the Asplund et al. (2009) solar abundances, and the Barber et al. (2006) water line lists. The broadband magnitudes we considered included $GG_{BP}G_{RP}$ from Gaia DR2, $Vgri$ from APASS, JHK_S from 2MASS, SDSS r_{iz} , and the WISE $W1$ and $W2$ passbands. We omitted UV flux measurements from our SED fit to avoid any possible bias induced by chromospheric UV excess; we similarly omitted WISE bands $W3$ and $W4$, but due to reliability concerns. astroARIADNE compares the measured broadband flux measurements against pre-computed model grids, and by default fits for six parameters: $\{T_{\text{eff}}, R_{\star}, A_V, \log g, [\text{Fe}/\text{H}], d\}$. The distance prior is drawn from Bailer-Jones et al. (2021). The surface gravity and metallicity are generally unconstrained. And finally, given our particular use-case, we assumed the following priors for the temperature, stellar size, and extinction:

$$T_{\text{eff}}/\text{K} \sim \mathcal{N}(3000, 1000), \quad (5)$$

$$R_{\star}/R_{\odot} \sim \mathcal{T}_{\text{N}}(0.5, 0.3, 0.1, 1.5), \quad (6)$$

$$A_V/\text{mag} \sim \mathcal{U}(0, 0.2), \quad (7)$$

for \mathcal{N} the Gaussian and \mathcal{U} the uniform distributions, and $\mathcal{T}(\mu, \sigma, a, b)$ a truncated normal distribution with mean μ , standard deviation σ , and lower and upper bounds a and b . We validated our chosen upper bound on A_V using a 2MASS color-color diagram. Finally, using Dynesty (Speagle 2020), we sampled the posterior probability assuming the default Gaussian likelihood, and set a stopping threshold of $d \log \mathcal{Z} < 0.01$, where \mathcal{Z} denotes the evidence.

With the effective temperatures and stellar radii from the SED fit, we then estimated the stellar masses by interpolating against the PARSEC isochrones (v1.2S Chen et al. 2014). The need for models that incorporate some form of correction for young, active M dwarfs is well-documented (e.g. Stassun et al. 2012; David & Hillenbrand 2015; Feiden 2016; Somers et al. 2020). Plausible explanations for anomalous M dwarf colors and sizes relative to model predictions include starspot coverage (e.g. Gully-Santiago et al. 2017), and potentially incomplete line lists (e.g. Rajpurohit et al. 2013). In the PARSEC models, Chen et al. (2014) performed an empirical correction to the temperature–opacity relation drawn from the BT-Settl model atmospheres, in order to match observed masses and radii of young eclipsing binaries. This is sufficient for our goal of estimating stellar masses. Given our observed $\{\tilde{T}_{\text{eff}}, \tilde{M}_{\star}, \tilde{t}\}$, and approximating their uncertainties as Gaussian $\sigma_{\tilde{T}_{\text{eff}}}$, $\sigma_{\tilde{M}_{\star}}$ and $\sigma_{\tilde{t}}$, we evaluate a distance d between our observations and any model PARSEC grid-point $\{T_{\text{eff}}, M_{\star}, t\}$ as

$$d^2 = \left(\frac{\tilde{T}_{\text{eff}} - T_{\text{eff}}}{\sigma_{\tilde{T}_{\text{eff}}}} \right)^2 + \left(\frac{\tilde{M}_{\star} - M_{\star}}{\sigma_{\tilde{M}_{\star}}} \right)^2 + \left(\frac{\tilde{t} - t}{\sigma_{\tilde{t}}} \right)^2, \quad (8)$$

in order to assign equal importance to each dimension. The preferred model mass is then one that minimizes this distance, and is quoted in Table 1. Uncertainties in the masses are propagated forward from the statistical uncertainties in the radii, temperatures, and ages.

3. RESULTS

3.1. CR catalog

Table 1 lists the 66 objects identified by our search. The “high-quality sample” includes 50 objects, which demonstrated what we viewed as unambiguous characteristics of the CR phenomenon in at least one TESS sector. The classification of 13 CR candidates was ambiguous, and the 3 remaining objects were false positives that we discuss below. The quality column in the table divides the three classes; additional data from TESS or other instruments could help resolve the classification of the ambiguous cases. Of the 63 CRs and candidate CRs, 32 were found using both the dip-counting and Fourier techniques, 23 were found using only the dip-counting technique, and 8 were found using only the Fourier technique. In the following, we will restrict our discussion to the high-quality sample, irrespective of discovery method.

The mosaic in Figure 4 shows phased light curves for the 50 CRs. The objects are sorted first in order of the number of TESS 120-second cadence sectors in which

¹ https://github.com/jgagneastro/banyan_sigma, git commit 394b486

² <https://github.com/adamkraus/Comove>, git commit 278b372

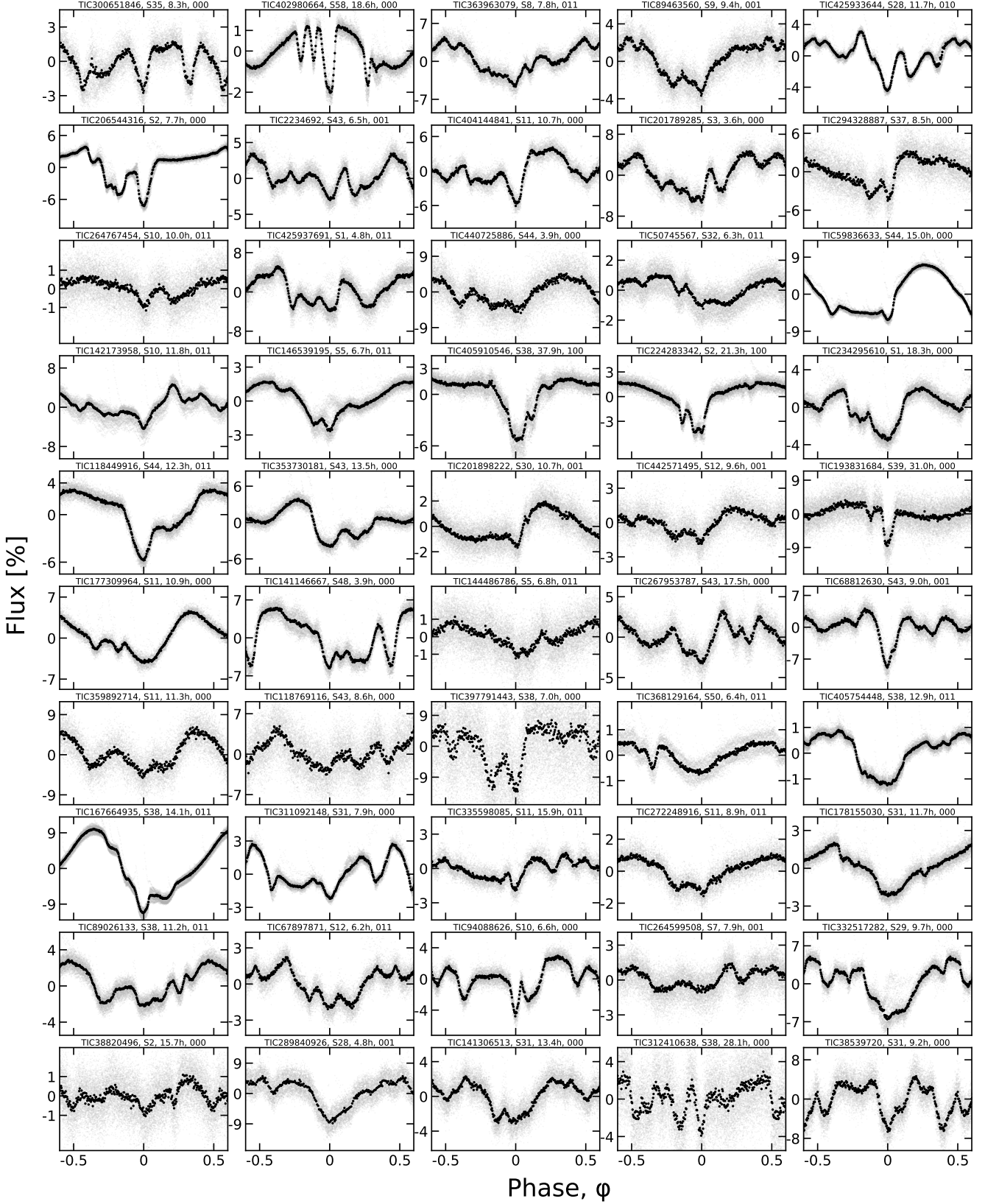


Figure 4. CRs found in the TESS 2-minute data. Phased TESS light curves over one month are shown for 50 CRs in the high quality sample. Gray are raw 2-minute data; black bins to 300 points per cycle. Objects are ordered such that sources with the most TESS data available are on top (see Section 3.1). Each panel is labeled by the TIC identifier, the TESS sector number, the period in hours, and the three-bit binarity flag from Table 1, which denotes Gaia DR3 radial_velocity_error outliers (bit 1), Gaia DR3 ruwe outliers (bit 2), and stars with secondary TESS periods (bit 3).

they clearly demonstrated the CR phenomenon, and secondarily by descending brightness. The top five objects by this metric are TIC 300651846 ($T=13.5$, 12 sectors); TIC 402980664 ($T=11.1$, 7 sectors); TIC 89463560 ($T=13.5$, 5 sectors); TIC 363963079 ($T=12.9$, 5 sectors); and TIC 294328887 ($T=14.2$, 4 sectors). The brightest five CRs span $9.3 < T < 11.1$; the faintest five span $14.5 < T < 15.0$. The fastest five have periods spanning $3.6 \text{ hr} < P < 6.2 \text{ hr}$, and the slowest five span $27 \text{ hr} < P < 38 \text{ hr}$.

In terms of the light curve shapes, Figure 4 shows a broad range of variability, with anywhere from two to eight local minima per cycle. Some stars show relatively ordinary modulation during one portion of the phased light curve, and highly structured modulation in the remainder of the cycle (e.g. TIC 206544316, TIC 224283342, TIC 402980664). Others show structured modulation over the entire span of a cycle (e.g. TIC 2234692, TIC 425933644, TIC 142173958). Others show some mix between these two modes.

A small number of objects at first glance seem reminiscent of eclipsing binaries, such as TIC 193831684, TIC 59836633, or TIC 5714469. We believe these cases are unlikely to be eclipsing binaries due to the additional coherent peaks and troughs in the light curves, which are distinct from any binary phenomena of which we are aware.

3.2. Ages

Of our 63 confirmed and candidate CRs, 61 were associated with a nearby moving group or open cluster, primarily using BANYAN Σ .³ The relevant groups are listed in Table 1; their ages span $\approx 5\text{-}200$ Myr. The most prodigious groups were Sco-Cen, Tuc-Hor, and Columba. Six CRs were also identified in the Argus association (Zuckerman 2019), which serves as an indirect line of evidence supporting the reality and youth of that group. The yield in Sco-Cen is not surprising since Sco-Cen contains the majority of pre-main-sequence stars in the solar neighborhood, and many of its stars were selected for TESS 120-second cadence observations by various guest investigators. Given the $\lesssim 10\%$ completeness of TESS beyond 100 pc, there may be many more CRs in Sco-Cen that remain to be discovered.

For the two stars for which BANYAN Σ did not find any association, we were not able to confidently associate either star with any young groups. Both do seem to show the CR signal over multiple TESS sectors, and both are photometrically elevated relative to the main sequence. Both were also noted by Kerr et al. (2021) as being in the “diffuse” population of < 50 Myr stars near the Sun.

Our search confirms that the CR phenomenon persists for at least ≈ 150 Myr. Table 1 includes three ≈ 150 Myr CRs in AB Dor (Bell et al. 2015), a ≈ 112 Myr old Pleiades CR (Dahm 2015), and a similarly-aged Psc-Eri member (Ratzenböck et al. 2020). To our knowledge, TIC 332517282

in AB Dor ($t=149^{+51}_{-19}$ Myr; Bell et al. 2015) was the previous record-holder for the oldest-known CR (Zhan et al. 2019; Günther et al. 2022); at least one unambiguous CR (EPIC 211070495) and a few other candidates were also previously known in the Pleiades (Rebull et al. 2016).

The upper age limit for CRs may even pass 200 Myr, based on the candidate membership of TIC 294328887 in the Carina Near moving group (Zuckerman et al. 2006). This group’s 200 ± 50 Myr age is based on the lithium sequence of its G-dwarfs (Zuckerman et al. 2006), which shows a coeval population of stars older than the Pleiades but younger than the 400 Myr Ursa Major moving group. The formal BANYAN- Σ membership probability is however somewhat low, perhaps due to the missing radial velocity. This lack of information could be resolved by acquiring even a medium-resolution spectrum. An independent assessment of the group’s kinematics using Gaia data, and its rotation sequence using TESS, could lend further credence in such an analysis.

3.3. Infrared excesses

Most CRs in our catalog did not show infrared excesses in the W1-W4 bands, which is typical for this class of object (Stauffer et al. 2017). Visually inspecting the SEDs of our 66 star sample and the WISE images available through IRSAs, we labeled two objects as having reliable infrared excesses (both W3 and W4 at $> 3\sigma$ above the photospheric prediction).

The two sources exhibiting an IR excess were TIC 193136669 (TWA 34) and TIC 57830249 (TWA 33). Both are in the TW Hydreae association (≈ 10 Myr), and have relatively long periods of 38 hr and 44 hr respectively. In our initial labeling, we labeled both as “ambiguous” CRs because the dips in their light curves did not show the rigid periodicity typical of CRs; their periods were also relatively long. However, inspection of further sectors clarified that both sources are dippers (see online plots in Figure 3). Independently, TIC 193136669 has a cold molecular disk based on observed 1.3 mm continuum emission and resolved Keplerian $^{12}\text{CO}(2-1)$ emission (Rodriguez et al. 2015). It was also labeled a dipper by Capistrant et al. (2022); we agree with their designation, and label it an “impostor” CR in Table 1. TIC 57830249 (TWA 33) also has previously detected 1.3 mm continuum emission (Rodriguez et al. 2015), suggestive of cold dust grains being present. It is also a dipper. Section 5.7 highlights plausible evolutionary connections between CRs and dippers in light of these “misclassifications” .

3.4. Binarity

The main types of binaries of interest in this work were those that were unresolved, because they could confuse our understanding of CRs. For instance, unresolved binaries might produce multiple photometric signals and hinder our ability to correctly identify the star hosting the CR signal. Unresolved binaries could also bias photometric magnitude and color measurements, which would affect our stellar parameter estimates. To attempt to identify binaries, we considered the following lines of information.

³ Two of the 61 memberships were made with low confidence and are flagged in Table 1. One membership, of TIC 397791443 in IC 2602, was made manually from a literature search (e.g. Cantat-Gaudin & Anders 2020).

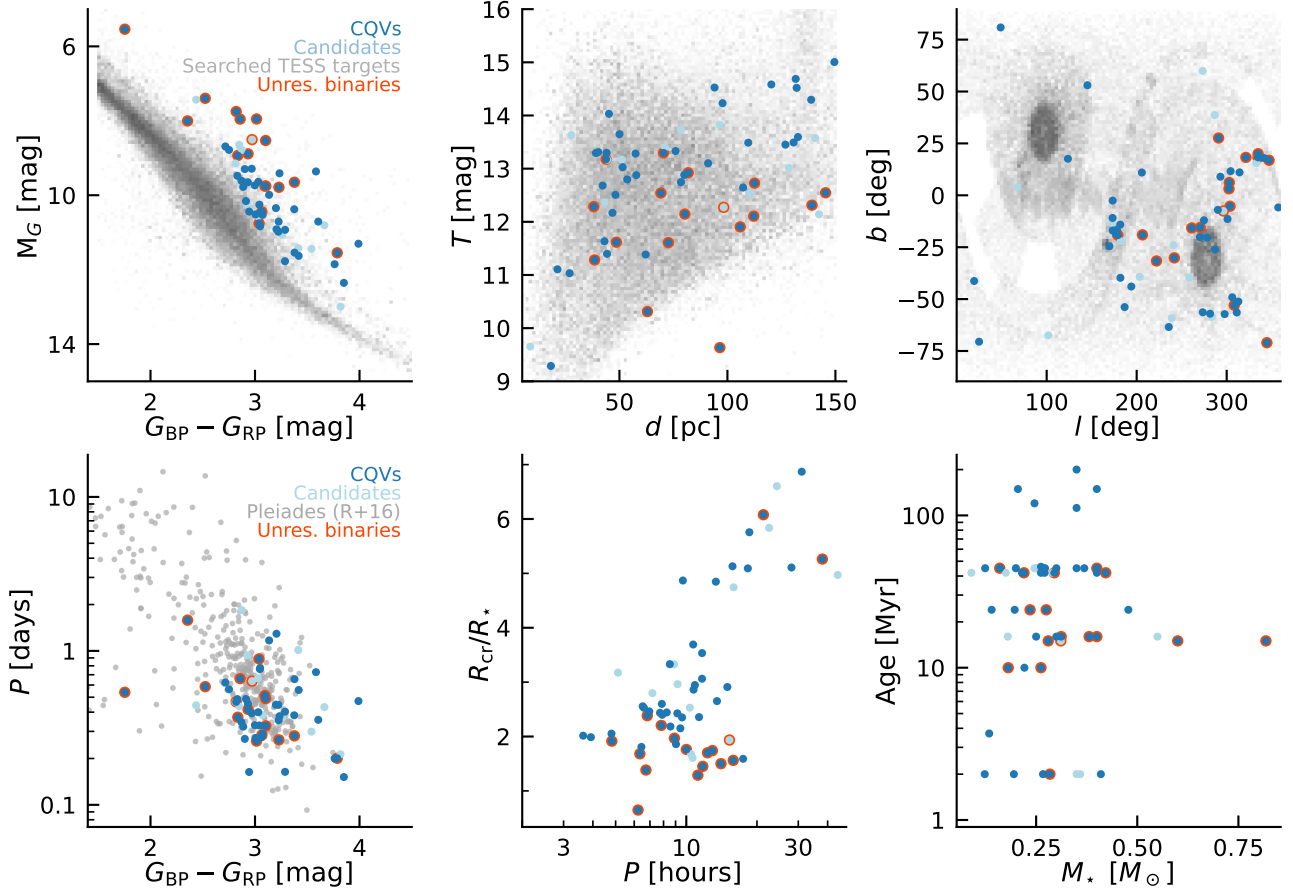


Figure 5. Properties of CRs identified by our search. CRs are mostly pre-main-sequence M dwarfs, younger than ≈ 150 Myr, with rotation periods faster than ≈ 1 day. The 50 bona fide CRs in Table 1 are the dark blue circles; 13 ambiguous CR candidates are light blue circles. Unresolved binaries are flagged either if the Gaia DR3 radial velocity scatter exceeded 20 km s^{-1} , or if $\text{Gaia RUWE}_{\text{DR3}} > 2$ and multiple photometric signals were present in the TESS light curve. The top panels show the 65,760 target stars with 120-second cadence TESS data as the shaded gray background; darker regions correspond to a larger relative number of searched stars. The lower-left panel compares the rotation–color distribution of CRs against the rotation periods of K and M dwarfs in the Pleiades from Rebull et al. (2016). The lower-middle panel plots the derived corotation radii $R_{\text{cr}} = (GM/\Omega^2)^{1/3}$ in units of stellar radii against the measured CR periods, in units of hours. Ages in the final panel are known from cluster membership.

Radial velocity scatter—We examined diagrams of the Gaia DR3 “radial velocity error” as a function of stellar color for all 63 CRs and candidate CRs. Since this quantity represents the standard deviation of the non-published Gaia RV time series, outliers can suggest single-lined spectroscopic binarity. These plots showed two clusters of stars, at $\lesssim 10 \text{ km s}^{-1}$ and $20\text{--}25 \text{ km s}^{-1}$. We therefore adopted a threshold of 20 km s^{-1} to flag possible single-lined spectroscopic binaries, which selected three stars: TIC 405910546, TIC 224283342, and TIC 280945693.

RUWE—We examined plots of Gaia DR3 RUWE as a function of color.⁴ Elevated RUWEs imply excess noise

relative to a single-source astrometric model. This can be caused by marginally resolved point sources skewing the single-transit centroid measurements, intrinsic photometric variability, or intrinsic astrometric motion. Based on this exercise, we adopted a threshold of $\text{RUWE}_{\text{DR3}} > 2$ to flag sources with excess astrometric noise. This threshold was met for 16/50 high-quality CRs; 0/13 of the ambiguous ones had this characteristic. There is some subjectivity in where to set the threshold, since the RUWE distribution has an extended tail (e.g. Penoyre et al. 2022). If we had instead required $\text{RUWE}_{\text{DR3}} > 1.4$, 21/50 high-quality CRs and 2/13 of the ambiguous sample would have been flagged.

Gaia DR3 non-single stars—Gaia DR3 included a `non_single_star` column that flagged eclipsing, astrometric, and spectroscopic binaries. None of the stars in our CR sample were identified as possible binaries in this column.

⁴ For an explanation of the renormalized unit weight error (RUWE), see the GAIA DPAC technical note http://www.rssd.esa.int/doc_fetch.php?id=3757412.

Multiple periodic TESS signals—During our visual analysis of the TESS light curves and PDM periodograms, we flagged sources with beating light curves, and with PDM periodograms that showed multiple periods. We also attempted to disentangle the two signals by subtracting the mean CR signal over each sector, and then repeating the phase-dispersion minimization analysis. The results of this effort are summarized in the secondary periods, P_{sec} , listed in Table 1, which we required to be at least 5% different from the primary period. This process yielded 22/50 high-quality CRs with secondary periods; 3/13 of the ambiguous sample met the same criterion. Of the 16 good CRs with $\text{RUWE}_{\text{DR3}} > 2$, 15 also showed secondary periods in the TESS light curves. Considering the weaker threshold of $\text{RUWE}_{\text{DR3}} > 1.4$, 18/21 such CRs showed secondary TESS periods.

Table 1 summarizes each of the above sources of information into a single bitwise column. We discuss possible connections between binarity and the CR phenomenon in Section 5.2.

4. CR EVOLUTION

4.1. Evolution over two year baseline

Figure 6 shows “before” and “after” views of 27 CRs for which TESS 120-second cadence observations were available at least two years apart. Such a baseline was available for 32 of the confirmed 50 CRs in our catalog; for plotting purposes we show the brightest 27. We have phased each sector to its own local minimum because for most of the sources we do not know the period at the precision necessary to be able to accurately propagate an ephemeris over two years. The achievable period precision, σ_P , can be estimated as

$$\sigma_P = \frac{\sigma_\phi P}{N_{\text{baseline}}}, \quad (9)$$

for N_{baseline} the number of cycles in the observed baseline and σ_ϕ the phase precision with which any one feature (e.g. a dip, or the overall shape of the sinusoidal envelope) can be tracked. Assuming $\sigma_\phi \approx 0.02$ and a 20-day baseline over a single TESS sector yields $\sigma_P \approx 0.25^{+0.38}_{-0.14}$ minutes for the population shown in Figure 6; propagated forward 1,000 cycles yields a typical ephemeris uncertainty range of 2–11 hours. Measuring the periods for each sector independently, there did not seem to be any significant ($>3\sigma$) period changes. This implies an absolute period stability of $\lesssim 0.1\%$ over the two-year baseline.

A few objects in Figure 6 show clear signs of the CR phenomenon in one sector, and marginal or non-existent signs in the other. While there is subjectivity in this assessment, to our eyes, cases for which at least one sector would be flagged as “ambiguous” include TIC 368129164 (Sector 23 might be labeled an EB), TIC 177309964 (Sector 38 would be simply a rotating star), TIC 404144841 (Sector 38 looks like a rotating star), TIC 201898222 (Sector 3 looks like a rotating star), TIC 144486786 (Sector 32 might be an RS CVn), and TIC 38820496 (Sector 28 might be an RS CVn). TIC 193831684, assessed on a single-sector basis, would

probably be labeled an eclipsing binary—in fact, Justesen & Albrecht (2021) already gave this source such a label. However, based on the shape evolution between Sectors 13 and 39, it is a CR. Based on the fraction of sources overall that “turned off”, the observed shape evolution implies that CRs have an on-off duty cycle of $\approx 75\%$. This type of correction is worth including in population-level estimates of how intrinsically common CRs are in the low-mass stellar population (e.g. Günther et al. 2022).

4.2. Evolution over adjacent sectors, & LP 12-502

A small fraction of our objects were in regions of sky with many sectors of adjacent TESS data. Out of this already small sample, LP 12-502 (TIC 402980664; $d=21\text{ pc}$, $J=9.4$, $T=11.1$) stood out due to the quality and content of its data. We discuss another interesting source, TIC 300651846, in Appendix B. In this section, we first present the LP 12-502 observations and then highlight their implications.

4.2.1. LP 12-502 observations

Figure 7 shows all available data for LP 12-502 from TESS Sectors 18, 19, 25, 26, 53, 58, and 59, split into successive orbits. The star was observed at 120-second cadence whenever it was observable by TESS. We binned the light curve to 15-minute intervals for visual clarity, and required at least one (120-second cadence) flux measurement per bin. Points more than 2.5σ above the median are drawn in gray, also for visual clarity. Missing data are not drawn. Figure 8 then shows the same data, but folded for each successive TESS orbit. Finally, Figure 9 shows “river plots” of the same data, split into similar intervals: the Sector 18-19 data, 25-26 data, 53 data, and 58-59 data. The river plots are subject to one additional processing step: we fitted and subtracted a maximum-likelihood two-harmonic sinusoid independently from the Sector 18-19 data, 25-26 data, and 53, 58, and 59 data in order to accentuate changes in the dip timing and structure.

The average period, determined by measuring the PDM peak period over each sector independently, was $\langle P \rangle = 18.5560\text{ hr}$. The range between the maximum and minimum sector-specific periods was measured to be about one minute. However, in detail, a period shift of ± 1 minute would yield major phase drifts over the baseline; that time interval corresponds to $\approx 1/1000^{\text{th}}$ of a period, and we have observed 1500 cycles. By fine-tuning over a grid in period, we found $P = 18.5611 \pm 0.0001\text{ hr}$, which seems to track certain features in the LP 12-502 light curve well over the entire dataset.

What exactly is observed? For the first 64 cycles, the star shows a pattern reminiscent of an eclipsing binary, with four obvious local minima. We dub these dips $\{1, 2, 3, 4\}$ at phases $\{-0.28, -0.08, 0, 0.25\}$, respectively. Over cycles 0–64, the depth of dips 1 and 3 remain roughly fixed. However dip 4 decreases in depth by about 2%, while dip 2 increases in depth, by about the same amount (see Figure 8). During cycles 48–64, a fifth dip may also be emerging, in the main “large” dip group.

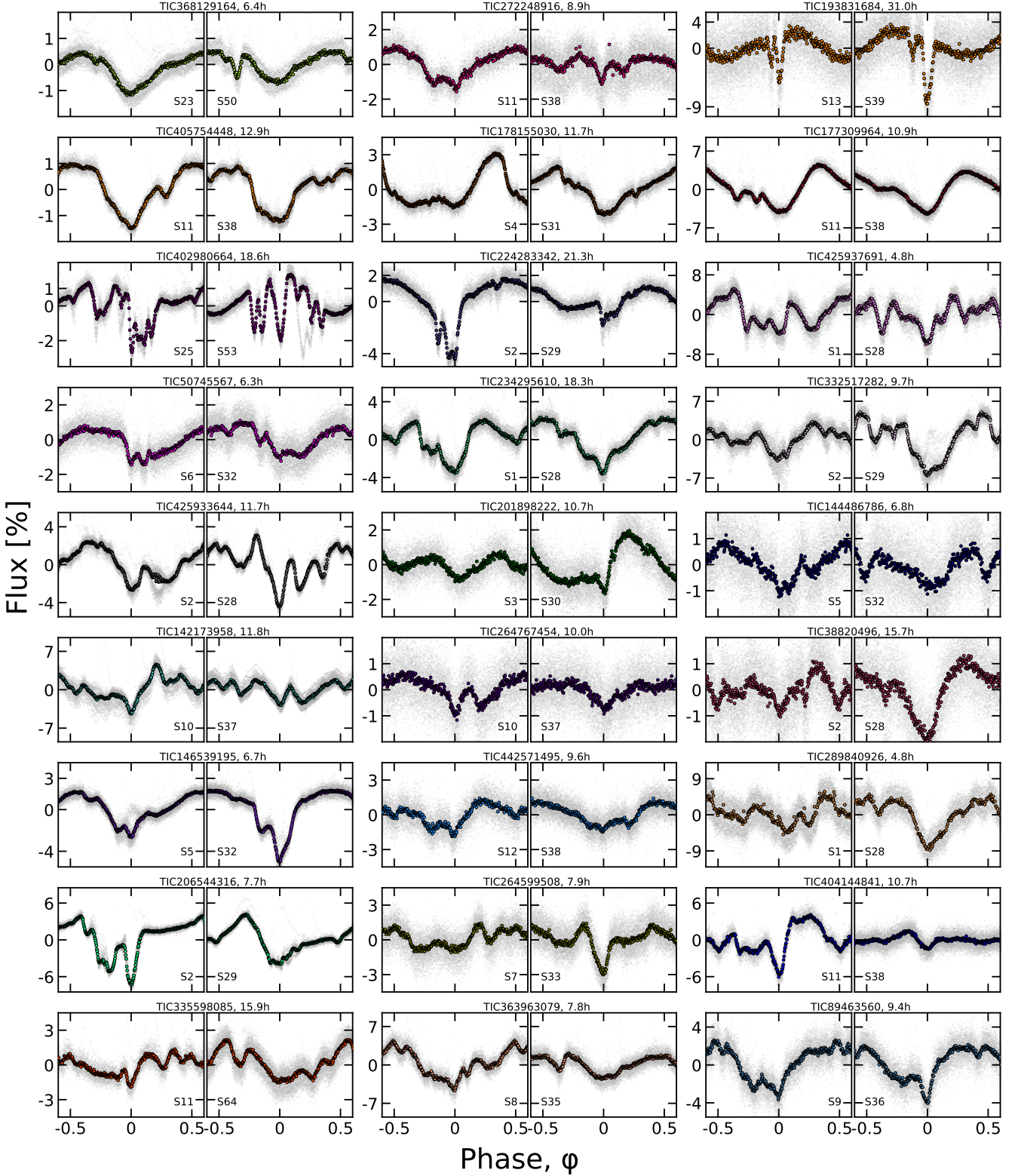


Figure 6. CRs keep their periods but change their shapes. Out of the 50 CRs in Figure 4, 32 had 120-second cadence TESS data available for a baseline of at least two years; the 27 brightest are shown here due to space constraints. Each panel shows one sector of TESS data, and is phased to its deepest minimum in flux. Each panel's title shows the TIC identifier and approximate period in hours. Text insets show the TESS sector numbers, which generally span two years, or at least 1,000 cycles. The vertical scale is fixed across sectors to clarify shape changes. Gray circles are raw 2-minute data; colored circles bin to 300 points per cycle.

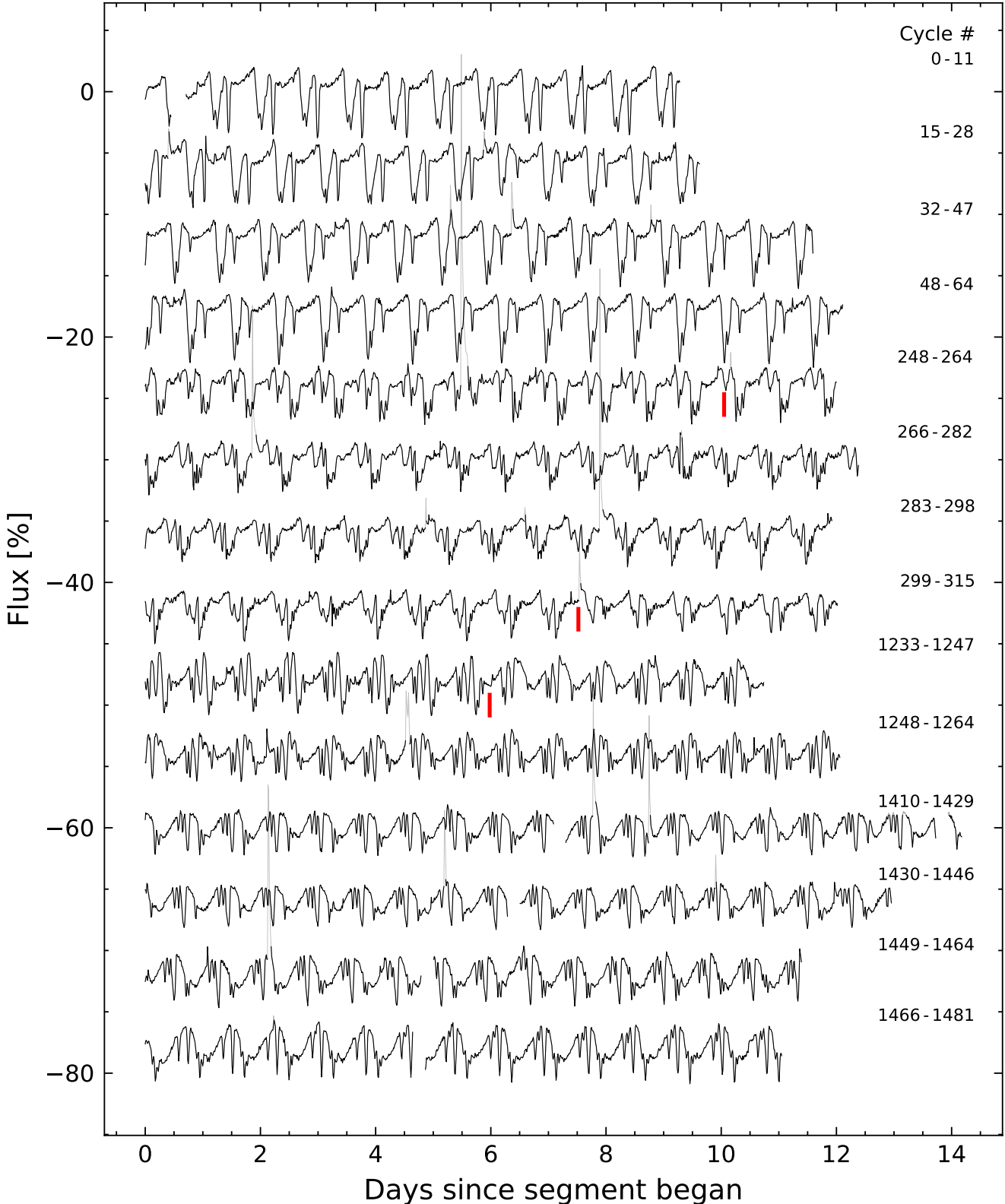


Figure 7. LP 12-502 (TIC 402980664) light curve, where each time segment represents one TESS orbit. Data were acquired in Sectors 18-19, 25-26, 53, and 57-58. Flares are drawn in gray. The light curve is binned to 15-minute intervals so that there are 96 points per day, and each point is connected by a line. Data gaps are not interpolated; if data are missing, nothing is plotted. The red vertical lines highlight apparently instantaneous state changes in the shape of the dip pattern.

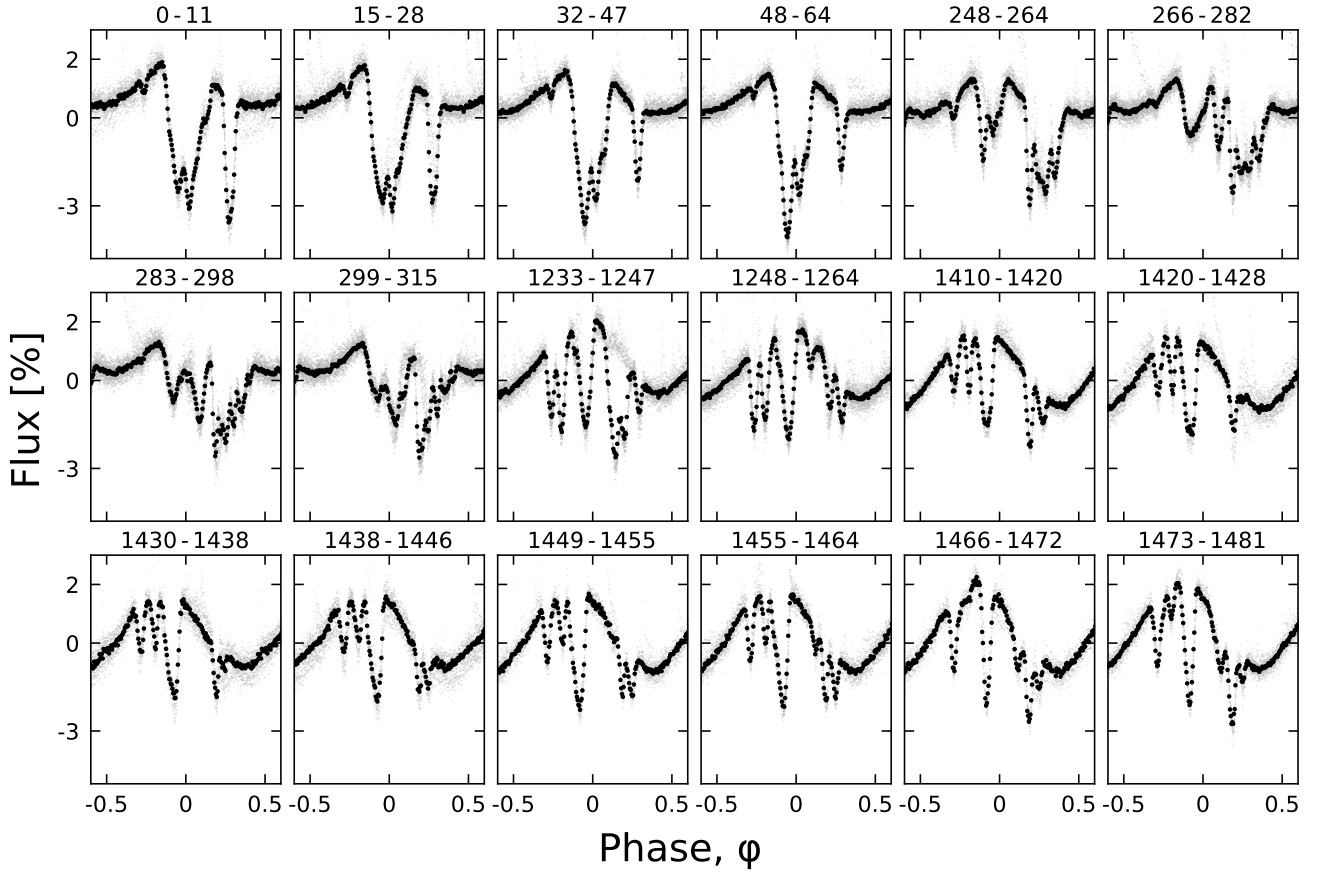


Figure 8. Evolution of LP 12-502 ($P=18.5611$ h) at fixed period and epoch over three years. Each panel shows one phase-folded TESS orbit; small text denotes relative cycle number. There are 200 binned black points per cycle. The TESS pointing law dictates the large time gaps between Cycles 64-248, 315-1233, and 1264-1410; larger gaps tend to yield larger shape changes. The dips usually evolve over tens to hundreds of cycles. However cycles 1233-1264 show a dip that “switched” from a depth and duration of 3% and 3 hr to 0.3% and 1 hr over less than one cycle (cf. Figure 7).

There is then a 6-month (184 cycle) gap to Cycles 248-315, which show two highly structured dip complexes, plus a small leading dip. The single leading dip is present at the same phase as in cycles 0-64, and is therefore likely to be the same structure. Along a similar line of logic, it seems plausible that the first “dip complex” during cycles 248-264 represents an evolution of the initial complex seen during cycles 0-64, though with reduced depth. During cycles 266-310, an additional local minimum develops between the two complexes; this feature is best visualized on the river plots (Figure 9), and we describe its (shorter) period below.

The second dip complex during cycles 248-315 shows the most substructure. During e.g. cycles 283-298, this single complex shows six local minima. The deepest dip is sharp: it shows a flux excursion of 3.5% over about 22 minutes ($0.02 P$), which is the steepest slope exhibited anywhere in the LP 12-502 dataset. After the sharp dip, there is a roughly exponential fall-off spanning about a quarter of a period, punctuated by coherent local minima and maxima which in detail (Figure 9) have slightly longer periods than the sharp dip. The sharp leading dip only decreases in depth follow-

ing a sudden state-switch at BTJD 2030.7 (cycles 299-315), which happens during a flare (Figure 7). The trailing dips remain thereafter.

Sectors 53–58 (cycles 1233-1481) are comparatively tame; they showed only four to six dips per cycle. Some dips remain stable in depth and duration over this five month interval. Other dips grow, like the one at $\phi = +0.06$ between cycles 1499 and 1481. Other dips, such as the one at $\phi = +0.12$ in cycles 1233-1264, disappear entirely. The most dramatic state switch occurs during cycles 1233-1247, when a large dip “switches” from a depth of 3% and duration of 3 hours to a depth of 0.3%, and a duration of 1 hour.

4.2.2. Lessons from LP 12-502

STATE-SWITCHES REVEAL DIP INDEPENDENCE—The state-switches seen in cycles 1233-1247 and 299-315 confirm that dips can disappear in less than one cycle, a point which has been previously appreciated (Stauffer et al. 2017). What is new in these particular changes is that the morphology changes show that the dips can be *independent* and *additive*. For example, throughout cycles 1233-1264, there are

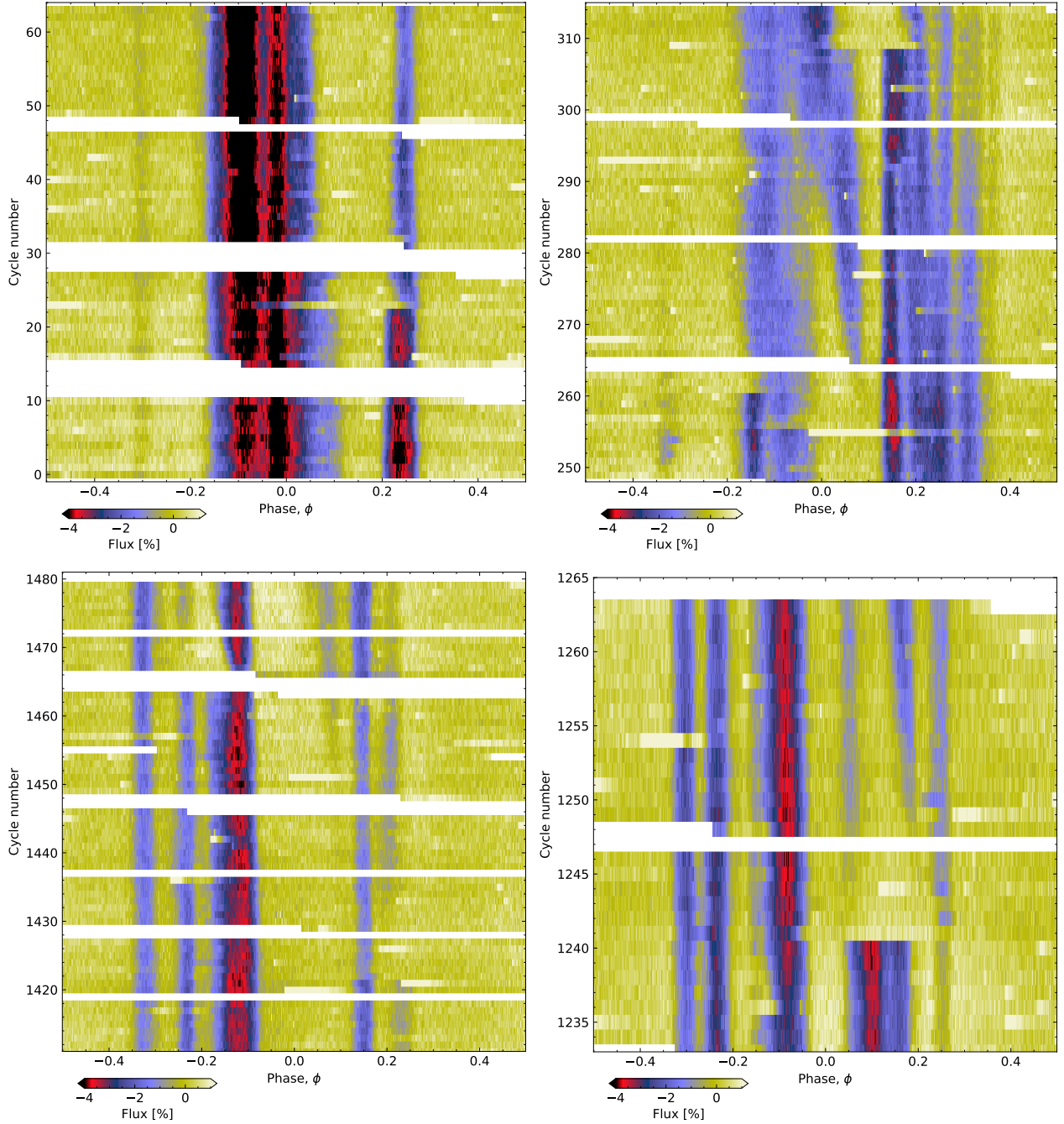


Figure 9. River plots of the LP 12-502 light curve, showing (clockwise from top-left) Sectors 18-19, 25-26, 53, and 58-59. A two-harmonic sinusoid has been subtracted to highlight the sharp dips. In Sectors 25-26 (cycles 248-315), periods are visible at the fundamental period of 18.5611 hr, as well as at faster ($\phi \approx 0-0.07$) and slower ($\phi \approx 0.25-0.27$) relative periods based on the presence of blue dips with distinct slopes. Multiple simultaneous periods are also visible in Sectors 53 and 58-59. White chunks denote missing data.

three local minima between phases of 0 and 0.3. They all have identical ingress times. The shape change during the transition implies that the leading dip that “turned off” (reduced its depth and duration), while the trailing two dips remained fixed. This is visible in Figure 8. In other words, the structures producing these dips are independent to the degree that one can undergo a severe change while the others remain identical. The state switches during cycles 248-264 and 299-

315 share the same characteristic: it is always the *leading* dip of a complex that “switches off”, leaving the (fixed-depth) trailing dips in its wake.

SLOW GROWTH; RAPID DEATH—Although there are a few instances in which we observe dips switch off over less than one cycle, dip growth seems to happen more slowly. For instance, the dip that grows between phase 0 and 0.1 between cycles 260-290 begins to become visible around BTJD

1993.2, and growths in depth by about 2% over about six cycles, to become visible by eye by BTJD 1997.7. The evolution of this particular dip is most clear in the river plots. The evolution of the latter dip group in cycles 1410-1481 is another example of this slow mode of dip growth.

DIP DURATIONS—The shortest dip duration for any of the individual LP 12-502 dips seems to be $\approx 0.06 P \approx 1.08$ hr. In comparison, using the stellar radius and mass derived in Section 2.3, the characteristic timescale $T_{\text{dur}} \equiv R_* P / (\pi a)$ for the transit of a point-source at corotation is 1.02 ± 0.10 hr. This means that while some of the LP 12-502 dips are sufficiently long to require structures that are extended in orbital azimuth, the durations of other dips are consistent with effective radii for the occulting material $R_{\text{eff}} \ll R_*$. This implies $a/R_* \approx 5.8$ for this material; the analogous timescale at the stellar surface is about six times slower.

DIP PERIODS—Most of the LP 12-502 dips repeat with a period of $P = 18.5611 \pm 0.0001$ hr. However the river plots (Figure 9) reveal that the light curve has specific dips with simultaneous but distinct periods. For instance, in sectors 25-26, the local minimum that develops around cycle 262 has a period faster than the mean period by $\approx 0.1\%$, while some of the trailing local minima in the main dip complex have periods slower than the mean period, by $\approx 0.04\%$. In addition to the fundamental period, we were able to identify at least four distinct periods shown by specific dips over the full Sectors 18-59 dataset, including periods at 18.5683, 18.5672, 18.5473, and 18.5145 hr, with a typical measurement uncertainty of ≈ 0.0002 hr. If each period corresponds to an individual dust or gas clump, then this implies that multiple distinct clumps can orbit the star simultaneously, at marginally different separations.

5. DISCUSSION

5.1. Typical and extreme CRs

Figure 5 shows derived stellar properties for our CR catalog, and compares the CRs against both the target star sample (top panels), and against stars in the Pleiades (Rebull et al. 2016). Typical CR masses span $0.1\text{-}0.4 M_\odot$, and typical ages span 2-150 Myr. This mass and age range includes both fully convective stars ($M_* \lesssim 0.25 M_\odot$), and stars with a combination of radiative cores and convective envelopes ($M_* \gtrsim 0.25 M_\odot$; Baraffe & Chabrier 2018). We found no obvious light curve morphology differences between the two classes. In terms of their rotation rates relative to the Pleiades, the CRs are among the more rapidly rotating half of M dwarfs.

The closest CR in our catalog is DG CVn (TIC 368129164; $d=18$ pc), a member of AB Dor. To our knowledge, this work is the first time that it has been noted as a CR. The three brightest CRs are DG CVn ($T=9.3$), TIC 405754448 ($T=9.6$), and TIC 167664935 ($T=10.3$). The shortest period belongs to TIC 201789285, at 3.64 hr. The longest period belongs to TIC 405910546, at 37.9 hr. If the latter source turns out to be an eclipsing binary, the next-longest would be TIC 193831684 (31.0 hr).

The lowest mass ($\approx 0.12 M_\odot$) belongs to TIC 267953787. The catalog contains a few other stars with similar mass. Given the small number of sub-stellar mass objects in our target sample, future studies of brown dwarf photometric variability might also yield CRs, though there could be degeneracies in interpretation with planetary surface features such as clouds and latitudinal bands (e.g. Apai et al. 2021; Vos et al. 2022).

5.2. CRs and binarity

5.2.1. Binary statistics

In Section 3.4, we found that a significant fraction of the CRs show indications of unresolved binarity. Excess noise above the Gaia single-source astrometric model is common (16/50 high-quality CRs with $\text{RUWE}_{\text{DR3}} > 2$), as is the presence of multiple periods in the TESS light curves (22/50). Elevated astrometric noise is almost always accompanied by multiple detectable TESS periods (15/16 high-quality CRs). The latter point strongly corroborates the idea that most sources with $\text{RUWE}_{\text{DR3}} > 2$ are intermediate separation binaries with projected apparent separations below 1'', and projected physical separations $\lesssim 50$ AU.

The multiplicity rate of M dwarfs near the Sun is $26.8 \pm 1.4\%$ (Winters et al. 2019). Based on the same study, the peak of the separation distribution decreases from ≈ 49 AU for $0.30\text{-}0.60 M_\odot$ stars, to ≈ 11 AU for $0.15\text{-}0.30 M_\odot$ M dwarfs. The multiplicity fraction in our CR sample seems either consistent or perhaps marginally higher than the field fraction. This could plausibly be understood in a physical framework in which the presence of intermediate-separation binaries causes early disk dispersal, freeing the star to contract. The CR phenomenon seems to require rapid rotation; thus if binary systems tend to produce more rapidly rotating stars, we would expect a sample of CRs to have a larger binary fraction than the field.

5.2.2. Do K dwarf CRs exist?

To date, the only stars reported to show the CR phenomenon are M dwarfs, with typical stellar masses $\lesssim 0.3 M_\odot$ (Stauffer et al. 2017; Günther et al. 2022). However the two most massive CRs in our sample, TIC 405754448 and TIC 405910546, appear to have masses of $\approx 0.82 M_\odot$ and $\approx 0.60 M_\odot$ respectively. The next-highest masses in our sample are $\approx 0.40 M_\odot$.

Based on their locations in the color–absolute magnitude diagram and membership in LCC, both of the K dwarfs do indeed appear to be high mass. However in detail, both are subject to ambiguities in interpretation. The TIC 405910546 light curve has a unique shape, suggestive of an eclipsing binary. Independently, TIC 405910546 was one of only three CRs flagged with a Gaia DR3 radial velocity scatter exceeding 20 km s^{-1} . Combined, these factors suggest that TIC 405910546 might be a pre-main-sequence eclipsing binary; it should be studied further to clarify this classification. For TIC 405754448, we believe that the source is an unresolved binary, because $\text{RUWE}_{\text{DR3}} = 6.8$, and because the

raw light curves in Sectors 11, 37, and 38 show an additional ≈ 6.5 day, $\approx 0.3\%$ amplitude sinusoidal signal suggestive of an unresolved photometric companion. If TIC 405754448 is a K+M binary, then the flux ratio between the primary and secondary would be expected to be $\approx 10:1$. It would be challenging for the M dwarf to produce the observed 12.9 hr signal with such a flux deficit, but not impossible. While both of these objects suggest that the CR phenomenon may extend up in mass to pre-main-sequence K dwarfs, more data are needed to fully substantiate this claim.

5.2.3. An astrophysical CR false positive: TIC 435903839

We originally classified TIC 435903839, with $\text{RUWE}_{\text{DR3}}=17.7$, as an “ambiguous” CR with a 10.8 hr period, because this period minimized the dispersion in the phase-folded light curve. More careful inspection however showed that it is an impostor: this source is a photometric blend of two ordinary rotating stars with $P_0=3.60$ hr, and $P_1=5.41$ hr, with a beat period $(P_0^{-1}-P_1^{-1})^{-1}$ of 10.8 hr. This is a novel false positive scenario for CRs: two rapidly-rotating stars with near-integer ratios of rotation periods. The beat between the two rotation signals produces the apparent CR signal. Such false positives can be excluded through careful accounting of all peaks in a periodogram. For instance, TIC 435903839 shows a peak at 16.27 hr, which is not an integer multiple of the dispersion-minimizing 10.82 hr period.

5.2.4. Multiple CRs in the same system: TIC 425937691 and TIC 142173958

TIC 142173958 and TIC 425937691 both show evidence for two separate CR signals in their TESS light curves. For TIC 142173958, the signals are at 11.76 hr and 12.84 hr. For TIC 425937691, they are at ≈ 4.82 hr and ≈ 3.22 hr, near the 3:2 commensurability. Given that both sources have two photometric signals and elevated RUWEs, they are probably unresolved binaries consisting of two independent CRs. Recent work has shown that the orbits of binaries closer than $\lesssim 700$ AU tend to be aligned with their planetary systems (e.g. Christian et al. 2022). If we assume that observing CR variability similarly requires near edge-on viewing geometries, then we might expect a sufficiently close binary with one CR to also have another, since the spin axes in sufficiently close binaries would tend to be aligned. In this scenario, the two periods of TIC 425937691 being within $\lesssim 1\%$ of the 3:2 period commensurability would simply be a coincidence.

5.3. CRs are quasiperiodic

A periodic signal repeats exactly; the CRs do not (Figure 6). While their periods appear to remain constant to within measurement precision over thousands of cycles, the light curve shapes evolve over 10 to 1,000 cycles. They are therefore *quasiperiodic*. While this observation is consistent with the analyses by Günther et al. (2022) and Popinchalk et al. (2023), it marks a qualitative departure from the “persistent” vs. “transient” flux dip distinction described by Stauff-

fer et al. (2017), since all CR dips seem to be transient over timescales of more than 1,000 cycles (Figure 6).

With that said, one might expect a truly quasiperiodic process to be able to explore all phase angles with equal weight. LP 12-502, and perhaps other CRs, seem to have preferred phases. For LP 12-502, all of the dips happen over phases corresponding to only two thirds of the period (Figure 8). The remaining third seems to be “out of limits” for any dipping material. This could be evidence that the stellar magnetic field is strongly asymmetric, and can hold extrinsic material at corotation, but only over two thirds of the equatorial circle. Alternatively, the source of the material (e.g. a planetesimal swarm) might be distributed over an arc of the same angular extent (240°). We favor the former explanation, for reasons discussed below.

5.4. Dip asymmetries and dust geometries

The asymmetry of a dip can help diagnose the optical depth of the occulting material as a function of orbital phase angle. Sharp leading edges with trailing exponential egresses for instance have been previously seen for transiting exocomets and disintegrating rocky bodies (e.g. Rappaport et al. 2012; Brogi et al. 2012; Vanderburg et al. 2015; Zieba et al. 2019).

Examining Figure 4, it is not obvious whether CRs as a whole show any preference for sharper ingresses, or sharper egresses. In some cases (e.g. TIC 425933644), the continuum itself is not well-defined, and so the meaning of “ingress” and “egress” are not clear. In others, such as Sector 36 of TIC 89463560, there is a single clear sharp ingress with an exponential egress, which could be fitted using e.g. a model analogous to those used for exocomets (e.g. Rappaport et al. 2018; Zieba et al. 2019). The main quantities of interest in such models would be the exponential decay time- and therefore length-scale, as well as the impact parameter and the inferred transit depth (and its implications for the equivalent “radius” of the transiting cloud). We briefly explored such models, until it became clear that careful modeling of sources such as LP 12-502 merits its own in-depth study. Connections could likely also be made to the toroidal geometries that can be produced by outflowing atmospheres of transiting planets (e.g. McCann et al. 2019; MacLeod & Oklopčić 2022).

5.5. Dust, or gas?

We believe that the most likely scenarios to explain CRs are either the dust clump scenario or the prominence scenario (Figure 1). Both invoke clumpy material that would be magnetically confined at the corotation radius. The prominence idea has a longer history, based on analogy with quiescent prominences/filaments observed to exist in the solar corona for up to a few weeks (see Vial & Engvold 2015). In an extrasolar context, spectroscopic detections of transient Balmer- and resonance-line absorption seen for stars such as AB Dor and Speedy Mic (e.g. Collier Cameron & Robinson 1989; Jeffries 1993; Dunstone et al. 2006; Leitzinger et al. 2016) led to the interpretation that the data could best be explained by similar structures: cold, minimally ionized hydro-

gen clouds or filaments that scatter chromospheric emission from the star to produce the observed spectroscopic line variations (see Collier Cameron & Robinson 1989). The short-term mechanical stability of such gas configurations is theoretically plausible (Ferreira 2000; Waugh & Jardine 2022), and the interpretation of this class of observations seems at least somewhat secure.

A clear link between the dense gas clumps (prominences) that likely exist around rapidly rotating low-mass stars and the CR phenomenon has yet to be made. A simple visual examination of the TESS light curves for five prominence-hosting systems studied by Jardine & Collier Cameron (2019)—AB Dor, Speedy Mic, LQ Lup, HK Aqr, and V374 Peg—revealed no obvious CR behavior, though all show differential evolution, and Speedy Mic shows two closely-spaced periods and a strong beat. Spectroscopically observable prominences do not imply photometric CR-like dips.

The key difference between the prominence and dust clump scenarios is in whether the occulting material of interest is neutral hydrogen, or dust. In the phrasing of the “frozen flux” condition of ideal rigid field magnetohydrodynamics, the tendency of both to become trapped at the corotation radius in the equatorial plane is tied to how of the four relevant forces (gravity, Lorentz, inertial Coriolis, and inertial centrifugal), the Lorentz and Coriolis only act perpendicular to field lines, while gravity and the centrifugal force are in balance at R_{cr} (see Townsend & Owocki 2005, Sec. 2). This assumes that the magnetic field dominates the flow, i.e., that $B^2/8\pi > \rho v^2/2$, so that matter is dragged along with the field lines. The locations where this condition holds may ultimately determine where matter can accumulate.

5.5.1. Gas absorption microphysics

CRs show broadband flux variations that can be 1-2× deeper in the blue than in the red (Onitsuka et al. 2017; Bouma et al. 2020; Günther et al. 2022; Koen 2023). For neutral hydrogen to produce this effect in absorption, its opacity must be larger in the blue than in the red. Gray (1992) suggests that this might be microphysically possible: while bound-bound absorption provides opacity only at narrow resonant lines, the hydrogen opacity due to bound-free absorption is “jagged” (see Gray 1992, Figure 8.5 and Eq. 8.8), such that at temperatures of $\approx 3,000$ K to $\approx 10,000$ K the observed chromaticities might be reproduced. While bound-free absorption of H⁻ seems like it should be important at such cool temperatures, in detail this opacity source has the *opposite sign* from what is required to produce deeper dips in the blue than in the red. Thomson scattering is similarly ruled out as a relevant opacity source, because it is gray. The final plausible alternative opacity source is dust, which has the requisite larger absorption cross-section in the blue than the red (Cardelli et al. 1989).

An instructive point of comparison is the rapidly rotating magnetic B star, σ Ori E, which shows dips that are deeper in the blue than in the red (Hesser et al. 1977). Photometric and spectroscopic observations of this star have been understood in terms of a warped torus of circumstellar material, analo-

gous to the geometries we are discussing for much cooler M dwarfs (Landstreet & Borra 1978; Nakajima 1985; Townsend et al. 2005). This material is unlikely to be dust, due to the relevant sublimation timescales. The opacity is instead thought to be sourced from bound-free absorption from neutral hydrogen (Nakajima 1985), although to our best knowledge direct evidence for this conclusion has yet to be acquired. Separate and smaller-amplitude emission in σ Ori E may also come from electrons scattering photospheric light toward the observer when the clouds are not in transit (Berry et al. 2022).

Given these complexities, it seems important for a future theoretical study to be conducted to determine to what degree the observed chromaticities in CRs match, or do not match, expectations from radiative transfer. This issue has a key ability to resolve the question of whether the CRs are explained by dust or by gas, which has bearing on whether the material producing the dips is coming from the star, or whether it is a byproduct of the protoplanetary disk.

5.5.2. The lifetime constraint

Independent of the microphysical basis for gas absorption, the observed lifetime of the CR phenomenon could provide another dimension to discern between the gas vs. dust clump scenarios. Based on the available statistics from e.g. Rebull et al. (2022) and references therein, it seems plausible that CR occurrence decreases in time, bottoming to zero well before the ≈ 700 Myr age of Praesepe. This is odd in the context of the prominence scenario, because pre-main-sequence M dwarfs spin up over the first $\approx 10^8$ yr; prominences might even be expected to be *more* common at the age of the Pleiades than for younger stars. This broadly assumes that any star that can support prominences will do so, and that the magnetic topology of rapidly rotating M dwarfs at 100 Myr is similar to that of rapidly rotating M dwarfs at say, 10 Myr. Based on the degree to which M dwarfs remain rapid rotators over the first few gigayears of their lives (e.g. Rebull et al. 2022; Pass et al. 2022), it seems surprising in the gas clump (prominence) scenario that very few stars older than 150 Myr have been seen to exhibit the phenomenon. In the dust clump scenario this is not a problem, because if the dust were externally sourced, it would be expected to have a finite supply.

5.6. Planets or planetesimal swarms near corotation?

Close-in planets are common around M-dwarfs; studies from Kepler have shown that high-mass M dwarfs have ≈ 0.1 planets per star with sizes between $1\text{-}4 R_{\oplus}$ and orbital periods within 3 days (Dressing & Charbonneau 2015). The number increases to ≈ 0.7 planets per star considering planets out to $P < 10$ days. Extrapolating to all small close-in planets with say $0.1\text{-}4 R_{\oplus}$ and within 10 days, it is reasonable to expect on average one close-in planet per M dwarf.

In the context of planet formation, the stopping location for the innermost planet is set by the location of the protoplanetary disk’s truncation radius (Izidoro & Raymond 2018). Although the disk truncation radius is defined by equating the

magnetic pressure from the stellar magnetosphere with the ram pressure from the inflowing gas, it also tends to coincide with the Keplerian corotation radius for low accretion rates (Hartmann et al. 2016; Li et al. 2022). Within models that have one or more planets migrating inward due to gas drag, the innermost planets therefore arrive at $\approx 5\text{-}10$ stellar radii before the disk becomes depleted.

Given the known abundance of small planets around M dwarfs, it is tempting to try to interpret features of the CR light curves in terms of the possible presence of either close-in exoplanets or close-in planetesimals. Rocky bodies this young could have molten global magma oceans analogous to those that existed on the Earth and Moon (see Lichtenberg et al. 2022), and could plausibly be outgassing either from those magma oceans, or from their unprocessed thin primordial atmospheres; in the former scenario, the gas would likely be enriched in heavy elements relative to the stellar wind. The system would in certain respects be analogous to the Jupiter-Io plasma torus (e.g. Saur et al. 2004), although with magnetic fields stronger by a factor of $\approx 1,000$. We emphasize that while this type of configuration seems a priori plausible, no direct evidence currently supports it.

The main logical function of the planetesimals is to serve as a source for the occulting gas or dust; they would not necessarily need to explain the observed phases of the observed dips. The azimuth angle of the eventual confinement could be entirely determined by the stellar magnetic field configuration. In this scenario, the obscuring material could potentially inspiral from outgassing planetesimals many stellar radii away from the corotation radius. While the planetesimals themselves would not necessarily need to transit, if they did, they would need to be $\lesssim 1 R_{\oplus}$ based on their non-detections in the TESS data. This would be analogous to previously known systems such as K2-22 (Sanchis-Ojeda et al. 2015) and KOI-2700 (Rappaport et al. 2014), though the obscuring material would be observed much further from the emitting planet.

A more restrictive variant of the planetesimal scenario would be to posit that the obscuring material remains close to the launching body, similar to comets, or to the aforementioned K2-22 and KOI-2700 systems. If so, then the planetesimals would need to be at the corotation radius. One prediction would therefore be that certain orbital phases would produce recurrent dips when observed over sufficiently long baselines, because the launching planetesimal would be massive enough to remain in orbit, while stochastically ejecting material. For most CRs (Figure 6), the data seem to be in tension with this expectation because the relative spacing between dips is almost never conserved. With that said, certain sources do seem to exhibit “special phases”, including LP 12-502 (TIC 402980664), DG CVn (TIC 368129164), TIC 193831684, and TIC 146539195. One possible explanation for this might be if obscuring material is remaining close to its launching body, or bodies. An alternative explanation could be that the stellar magnetic field configurations responsible for confining said material are stable over the existing two-year baseline.

5.7. From dippers to debris disks

In identifying the two candidate CRs with outlying SEDs (TICs 193136669 and TIC 57830249; Section 3.3), we were prompted to reconsider our light curve-based labeling, and ultimately concluded that these sources are dippers. This episode suggests that there could be overlap between CRs and dippers. It is also worth emphasizing that our labeling of e.g. TIC 57830249 was based on a single sector of TESS data (Sector 36) when its behavior was relatively periodic and it showed dip depths of a few percent. However, in other TESS sectors (e.g. Sector 10), this source looks completely different, varying in apparent flux by a factor of two, with no discernible periodicity at all.

Assessing these results against the backdrop of our increasing understanding of dippers (e.g. Cody et al. 2014; Ansdell et al. 2016; Robinson et al. 2021; Capistrant et al. 2022; Gaidos et al. 2022), it is clear that the loss of an infrared excess is associated with strong changes in a star’s optical variability. It is reasonable to imagine connections between CRs and dippers: both classes of object can show transient flux dips that are relatively narrow in duration. The dips in both are probably associated with clumps of dust or gas. However the CR dips are generally more periodic and less deep than those of dippers; they also display far less transience over timescales of a few to tens of cycles. The CRs also have demonstrably less dust than (most) dipper stars. At a population level, the CR stars are also older. A common mystery between the CRs and dippers, in our own estimation, is how exactly the narrowness of the dust clumps is produced. It is not unreasonable to imagine a similar mechanism operating for both types of object, tied perhaps to a shared magnetic topology, or perhaps to a preference for dust to inspiral to the star in clumped structures.

5.8. Mass flux estimate

We can estimate the mass of a transiting cloud by first converting the transit depth to an effective cloud radius, R_{cloud} . For most CRs in Figure 4, this yields $\approx 2\text{-}20 R_{\oplus}$. A minimum constraint on the number density follows by requiring the cloud to be optically thick. For cases like LP 12-502, this is reasonable because the transit duration of the shortest dips implies $R_{\text{cloud}} \ll R_{\star}$. Carrying out the relevant calculation assuming the occulting material is dust grains $1 \mu\text{m}$ in size, Sanderson et al. (2023) reported minimum cloud masses of order 10^{12} kg (their Eq. 23), which scale linearly with both the optical depth and dust grain radius. This is comparable to a small asteroid; the asteroid belt itself has a mass of order $\approx 10^{21} \text{ kg}$ (Park et al. 2019). If the material were cool gas prominences rather than dust, the mass would need to be of order 10^{14} kg (Collier Cameron et al. 1990), about $100\times$ larger than the requisite dust mass.

Our observations provide a direct measurement of how often dips appear and disappear, both due to sudden state-switches, and due to more gradual, secular evolution. For instance, LP 12-502 showed three “state-switch” events over the six months of available TESS observations, during cycles 248-264, 299-315, and 1233-1247. In each case, a dip

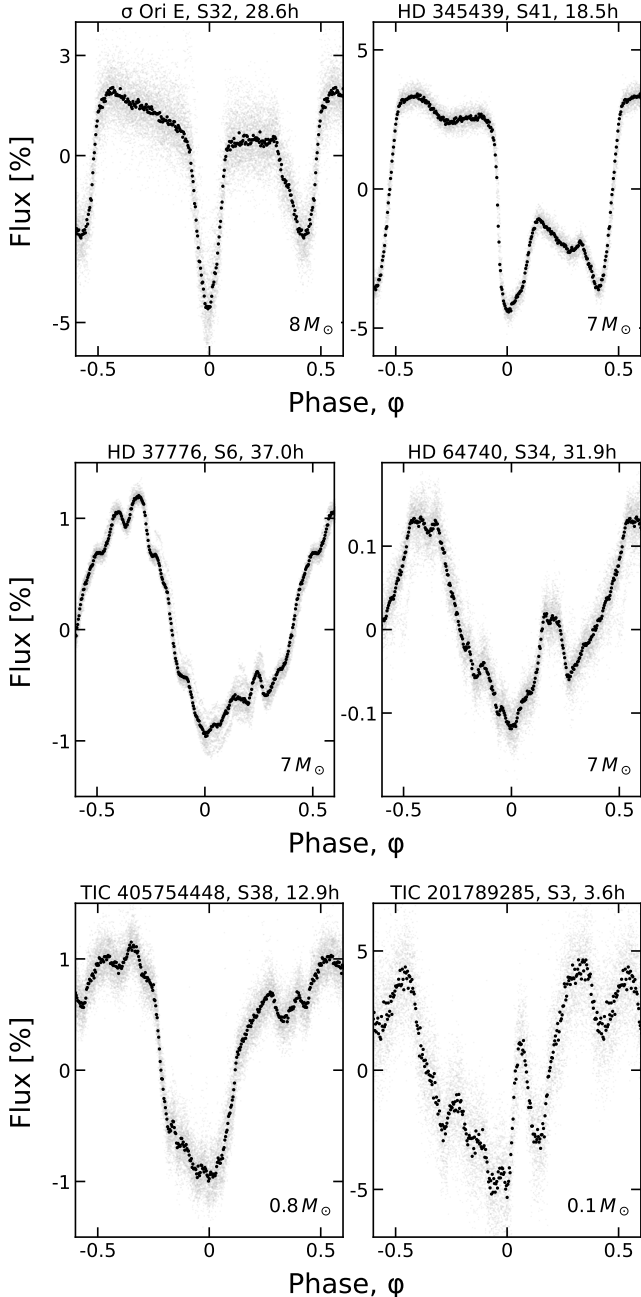


Figure 10. **The magnetic B star connection.** σ Ori E and HD 345439 (top row) are magnetic B stars with predominantly dipolar magnetic fields known to host circumstellar plasma tori. HD 37776 and HD 64740 (middle row) are analogous magnetic B stars with field topologies dominated by high order multipoles. The bottom row compares the latter systems against the “best-matching” CR light curves, selected by eye from Figure 4. CRs have light curves that are visually similar to the topologically complex magnetic B stars. Stellar masses rounded to one significant figure are given in the lower right of each panel; the star, TESS sector, and period are listed in each subtitle.

“turned off”. It is plausible to imagine that these events correspond to either mass being ejected from the corotating clumps, or else perhaps being accreted onto the star. In either case, the corresponding $\dot{M} \equiv M \cdot dN/dt$ time-averaged over six months is $\approx 3 \times 10^{-18} M_{\odot} \text{ yr}^{-1} \approx 1 \times 10^{-12} M_{\oplus} \text{ yr}^{-1}$. Considered cumulatively over the $\approx 10^8$ years for which the CR phenomenon is observed, this yields a cumulative moved dust mass of $10^{-4} M_{\oplus}$, of order the Solar System’s asteroid belt. If the occulting material is gas, the masses involved would be of order 100 times larger. For cases in which we observe the *growth* of dips, such as the Sector 29 data for TIC 224283342, or Sector 5 of TIC 294328885, the dip depths typically increase by of order a few percent over ten to twenty days. This growth rate yields a mass flux one order of magnitude larger than the earlier estimate.

5.9. Strengthening the magnetic B star connection

Stauffer et al. (2017) previously noted a possible connection between the CRs and rapidly rotating magnetic B stars such as σ Ori E, which can have circumstellar gas clouds trapped in corotation (Townsend et al. 2005). The σ Ori class is distinct from Be-star decretion disks, which do not have any obvious connection to the stellar magnetic field (Rivinius et al. 2013).

An argument against the connection between CRs and the σ Ori E analogs is that the light curve of σ Ori E is much simpler than those in Figure 4, with only two broad local minima, and one “hump” (Figure 10; see also Jayaraman et al. 2022). Within the model proposed by Townsend et al., this is explained by the simplicity of the star’s magnetic field, which is well-approximated by a dipole, similar to most other magnetic B stars (Aurière et al. 2007; Donati & Landstreet 2009). The magnetic axis needs to be tilted relative to the stellar spin axis in order to match the qualitative behavior of both the broadband light curves, and the line-profile variations seen in hydrogen, helium, and carbon (Oksala et al. 2012).

Two exceptions to the rule of “simple field topologies for magnetic B stars” are HD 37776 and HD 64740, which are B stars that were previously known from spectropolarimetry to have field geometries dominated by high order multipoles (Kochukhov et al. 2011). Reviewing the literature, we learned that recent TESS light curves of these two B stars appear surprisingly similar to the CR light curves (Mikulášek et al. 2020). The middle row of Figure 10 shows the phased TESS light curves for these two outlying magnetic B stars, with by-eye “best matching” CRs shown underneath for comparison. The number of dips per cycle, the shapes of the dips, and the dip depths relative to the sinusoidal envelope all appear to be similar. This surprising connection suggests that the highly-structured M dwarf light curves may imply multipolar magnetic fields – since it is the complex fields which are the defining characteristic of these two B stars, relative to other known magnetic B stars like σ Ori E. This is consistent with the non-axisymmetric topologies that have been reported in a small number of M dwarfs for which Zeeman Doppler Imaging is technically feasible (see Kochukhov 2021, and references therein).

The physical similarity between the B stars and the M dwarfs presumably has its origin in the existence of a “centrifugal magnetosphere” (see Petit et al. 2013). In other words, both classes of objects probably satisfy the condition $R_M > R_{cr}$, for R_M the magnetospheric radius (sometimes referred to as the Alfvén radius). When this condition holds, stable points exist wherever the outward centrifugal force is balanced by the combined effect of gravity and magnetic tension along closed field loops (Nakajima 1985). In the converse “dynamical” case, when $R_M < R_{cr}$, material interior to the magnetospheric radius returns to the stellar surface over the free-fall timescale. A simple estimate assuming a dipole field with $B_0 \approx 1\text{ kG}$ at the star’s surface, a local plasma number density $n \approx 10^9\text{ cm}^{-3}$, and a plasma temperature 10^6 K gives magnetospheric radii of order a few times the corotation radii, R_{cr} . This suggests that the existence of a centrifugal magnetosphere is plausible in young, rapidly rotating M dwarfs.

6. CONCLUSIONS

In this work, we searched 120-second cadence TESS data collected from 2018 July to 2022 September for complex rotators (CRs). The target stars were 65,760 K and M dwarfs within 150 pc. The selection function was $>80\%$ complete within 30 pc, and $<10\%$ complete at distances exceeding 100 pc.

In our target sample, we found 50 objects that showed complex quasiperiodic behavior over at least one TESS sector. These 50 bona fide CRs are listed in Table 1. This table also includes an additional 13 ambiguous CRs, whose designation is less certain, and 3 impostors. We inferred ages for all but two of the 66 objects based on association memberships; we also derived temperatures and radii using SED fitting, and then inferred stellar masses by interpolating against stellar evolutionary models. We caution that our selection function was not volume-limited: the TESS 120-second stellar sample had a heterogeneous selection function which may have been biased in favor of young stars over field stars. Previous work however has shown that $\approx 1\text{-}3\%$ of M dwarfs younger than $\approx 100\text{ Myr}$ show the CR phenomenon (Rebull et al. 2016; Günther et al. 2022).

Analyzing the TESS light curves and stellar properties of our CRs, we draw the following conclusions.

1. CRs are quasiperiodic. The mean periods remain fixed over the $>1,000$ -cycle baseline of available observations; but the light curve shapes always evolve (Figure 6).
2. The same CR can show multiple periods simultaneously. LP 12-502, for instance, showed dips with four distinct periods within $\pm 0.3\%$ of its fundamental period, sometimes simultaneously, and each lasting for up to 50 cycles (Figure 9).
3. CRs evolve over timescales that are both secular (>100 cycles) and impulsive (<1 cycle). Dip growth seems to happen over durations of at least ten cycles, and

slow dip decay can also occur. “State-switches” correspond to dips collapsing instantaneously, and are almost always linked with observed optical flares. This suggests that the occulting material is sensitive to sudden changes in the magnetic field.

4. The rate of dip evolution can be used to place a model-dependent constraint on how much material is either being accreted or ejected during the state changes (Section 5.8). Order of magnitude estimates require at least an asteroid belt’s worth of dust ($10^{-4} M_\oplus$) over 10^8 years, or $\approx 10^{-2} M_\oplus$ if the occulting material is gas.
5. The CR phenomenon persists for $\gtrsim 150\text{ Myr}$, based on the existence of multiple CRs in AB Dor, the Pleiades, and Psc-Eri (Section 2.3). It may even extend to 200 Myr, based on the one CR we found in the Carina Near moving group (TIC 294328887; $\approx 200\text{ Myr}$). However the lack of detected CRs in the Hyades and Praesepe suggests that the lifetime of the phenomenon is limited to the first few hundred million years.
6. The on-off duty cycle for CRs seems to be $\approx 75\%$, based on the fraction of bona fide CRs that either turned on or turned off during TESS re-observations, two years after the initial observation (Figure 6).
7. Most CRs are M dwarfs with masses $0.1\text{-}0.5 M_\odot$. Two sources, TIC 405754448 and TIC 405910546, have masses that appear to exceed the M dwarf limit. However both are potentially binaries, and this may confuse our ability to accurately identify the source of the CR signal (Section 5.2.2). We encourage additional scrutiny of these objects in future work.
8. Surprising analogs to the CRs exist in magnetic B stars, but only those with multipolar field topologies. Since most magnetic B stars have dipolar magnetic fields, this suggests that the CR dips and warps are similarly being sculpted by the stellar magnetic fields, and that the magnetic fields themselves are probably also multipolar.
9. The closest CRs to the Sun are at distances of 15–20 pc, and the brightest have $V \approx 12$ ($J \approx 7.5$). We have found most of them in this work, since our CR sample was $\gtrsim 80\%$ complete within 30 pc. The lack of CRs in the volume-complete <15 pc sample of $0.1\text{-}0.3 M_\odot$ stars analyzed by Winters et al. (2021) is consistent with this estimate. Expanding our analysis of the TESS data to the full frame images would yield a truly volume-limited selection function, and would expand the CR census by about a factor of two within 50 pc, and by a factor of ten within 100 pc.

While many questions remain, two in particular will be important for clarifying what these objects might teach us in a broader astrophysical context: 1) Is the eclipsing material responsible for the phenomenon gas or dust? 2) What sets the characteristic clumping size for the circumstellar material?

The distinction between gas or dust is important because it will clarify whether the CR phenomenon is intrinsic, so that material comes from the star, or extrinsic, so that it is sourced through some generic evolutionary phase of debris disks. This knowledge would in turn propagate to our understanding of whether the phenomenon is primarily teaching us about dust production and processing in gas-poor disks, or whether it is teaching us about the ability of cold gas to remain stable in hot stellar coronae for long durations. Observationally, acquisition of medium- or high-resolution time-series spectra holds a good chance at resolving the gas vs. dust question. Given our observed $\approx 75\%$ on-off duty cycles, such data must be acquired simultaneously with photometric time-series observations (e.g. during TESS re-observation) in order for detections and non-detections to be interpretable.

In both the gas and dust scenarios, CRs are preferentially viewed edge-on. This implies that after correcting for the line-of-sight inclination, roughly one third of low mass stars (those that rotate rapidly enough; [Günther et al. 2022](#)) could trap circumstellar material in the same way. It also suggests that CRs may preferentially show transiting planets at larger distances than the corotating material, though this may be dependent on whether the magnetic and stellar spin axes tend to be aligned. Given these points, observational follow-up work should include searching for outer transiting planets, and measuring equatorial velocities in order to test whether the stellar inclination angles are indeed preferentially edge-on. Any source of empirical information on the stellar magnetic field, whether from the Zeeman effect (e.g. [Kochukhov 2021](#)) or perhaps radio emission (e.g. [Hallinan et al. 2015](#)), could also help clarify the strength of the magnetospheres for these objects.

On the theoretical front, building a physical understanding what sets the characteristic size scale of the clumping material would help clarify why the light curves have the bizarre shapes that are observed. The relevant puzzles in plasma physics and radiative transfer could perhaps be connected to our understanding of the close-in rocky planets that are expected to be present around most of these stars. The challenges intrinsic to both the observational and theoretical work seem worth the effort.

ACKNOWLEDGMENTS

LGB is grateful for support from the Heising-Simons 51 Pegasi b Fellowship, and for helpful conversations with G. Laughlin, A. Mann, and J. Spake. This paper relied on data collected by the TESS mission, which are publicly available from the Mikulski Archive for Space Telescopes (MAST). The specific 120-second cadence observations can be accessed via [DOI](#). Funding for the TESS mission is provided by NASA's Science Mission Directorate. TIC 402980664 in particular was observed at 120-second cadence thanks to the TESS Guest Investigator programs G022252 (PI: J. Schlieder; Sectors 18, 19, 25, 26) and G04168 (PI: R. Jayaraman; Sector 53).

LGB conceived the project and performed the dip-counting search, light curve classification, cluster membership, SED, variability, and secondary-period analyses. RJ and SR performed the Fourier-based analysis and contributed to light curve classification. LR cross-examined the light curve classification, and contributed an independent SED analysis. AD identified the magnetic B star connection. LAH contributed to project design and to the interpretation of the light curves. GAB acquired and maintained the servers used to run the dip-finding pipeline. — **JNW, MNG, GRR to confirm coauthorship &/or to help out on interpretation!** All authors assisted in manuscript writing and revision.

Software: astrobase ([Bhatti et al. 2021](#)), astropy ([Astropy Collaboration et al. 2013, 2018, 2022](#)), lightkurve ([Lightkurve Collaboration et al. 2018](#)), numpy ([Harris et al. 2020](#)), pyGAM ([Servén & Brummitt 2018](#)), scipy ([Virtanen et al. 2020](#)), TESS-point ([Burke et al. 2020](#)), wotan ([Hippke et al. 2019](#)).

Facilities: *Astrometry*: Gaia ([Gaia Collaboration et al. 2018, 2022](#)). *Imaging*: Second Generation Digitized Sky Survey. *Spectroscopy*: Keck:I (HIRES; [Vogt et al. 1994](#)). *Photometry*: TESS ([Ricker et al. 2015](#)), *Broadband photometry*: 2MASS ([Skrutskie et al. 2006](#)), APASS ([Henden et al. 2016](#)), Gaia ([Gaia Collaboration et al. 2018, 2022](#)), SDSS ([York et al. 2000](#)), WISE ([Wright et al. 2010](#)).

REFERENCES

- Allard, F., Homeier, D., & Freytag, B. 2012, *Philosophical Transactions of the Royal Society A: Mathematical, Physical and Engineering Sciences*, 370, 2765
- Ansdell, M., Gaidos, E., Rappaport, S. A., et al. 2016, *ApJ*, 816, 69
- Apai, D., Nardiello, D., & Bedin, L. R. 2021, *ApJ*, 906, 64
- Asplund, M., Grevesse, N., Sauval, A. J., & Scott, P. 2009, *ARA&A*, 47, 481
- Astropy Collaboration, Robitaille, T. P., Tollerud, E. J., et al. 2013, *A&A*, 558, A33
- Astropy Collaboration, Price-Whelan, A. M., Sipőcz, B. M., et al. 2018, *AJ*, 156, 123
- Astropy Collaboration, Price-Whelan, A. M., Lim, P. L., et al. 2022, *ApJ*, 935, 167
- Aurière, M., Wade, G. A., Silvester, J., et al. 2007, *A&A*, 475, 1053
- Bailer-Jones, C. A. L., Rybizki, J., Fouesneau, M., Demleitner, M., & Andrae, R. 2021, *AJ*, 161, 147
- Baraffe, I., & Chabrier, G. 2018, *A&A*, 619, A177
- Barber, R. J., Tennyson, J., Harris, G. J., & Tolchenov, R. N. 2006, *MNRAS*, 368, 1087
- Basri, G. 2021, An Introduction to Stellar Magnetic Activity
- Bell, C. P. M., Mamajek, E. E., & Naylor, T. 2015, *MNRAS*, 454, 593
- Berry, I. D., Owocki, S. P., Shultz, M. E., & ud-Doula, A. 2022, *MNRAS*, 511, 4815
- Bhatti, W., Bouma, L., Joshua, et al. 2021, waqasbhatti/astrobase: astrobase v0.5.3, Zenodo
- Bodman, E. H. L., Quillen, A. C., Ansdell, M., et al. 2017, *MNRAS*, 470, 202
- Bouma, L. G., Winn, J. N., Ricker, G. R., et al. 2020, *AJ*, 160, 86
- Bouma, L. G., Curtis, J. L., Masuda, K., et al. 2022, *AJ*, 163, 121
- Bressan, A., Marigo, P., Girardi, L., et al. 2012, *MNRAS*, 427, 127
- Briceño, C., Calvet, N., Hernández, J., et al. 2019, *AJ*, 157, 85
- Brogi, M., Keller, C. U., de Juan Ovelar, M., et al. 2012, *A&A*, 545, L5
- Burke, C. J., Levine, A., Fausnaugh, M., et al. 2020, TESS-Point: High precision TESS pointing tool, Astrophysics Source Code Library, record ascl:2003.001
- Cantat-Gaudin, T., & Anders, F. 2020, *A&A*, 633, A99
- Capistrant, B. K., Soares-Furtado, M., Vanderburg, A., et al. 2022, *ApJS*, 263, 14
- Cardelli, J. A., Clayton, G. C., & Mathis, J. S. 1989, *ApJ*, 345, 245
- Chen, Y., Girardi, L., Bressan, A., et al. 2014, *MNRAS*, 444, 2525
- Christian, S., Vanderburg, A., Becker, J., et al. 2022, *AJ*, 163, 207
- Cody, A. M., Stauffer, J., Baglin, A., et al. 2014, *AJ*, 147, 82
- Collier Cameron, A. 1999, in *Astronomical Society of the Pacific Conference Series*, Vol. 158, Solar and Stellar Activity: Similarities and Differences, ed. C. J. Butler & J. G. Doyle, 146
- Collier Cameron, A., Duncan, D. K., Ehrenfreund, P., et al. 1990, *MNRAS*, 247, 415
- Collier Cameron, A., & Robinson, R. D. 1989, *MNRAS*, 238, 657
- Curtis, J. L., Agüeros, M. A., Mamajek, E. E., Wright, J. T., & Cummings, J. D. 2019, *AJ*, 158, 77
- Dahm, S. E. 2015, *ApJ*, 813, 108
- David, T. J., & Hillenbrand, L. A. 2015, *ApJ*, 804, 146
- Donati, J. F., & Landstreet, J. D. 2009, *ARA&A*, 47, 333
- Dressing, C. D., & Charbonneau, D. 2015, *ApJ*, 807, 45
- Dunstone, N. J., Barnes, J. R., Collier Cameron, A., & Jardine, M. 2006, *MNRAS*, 365, 530
- Fausnaugh, M., Morgan, E., Vanderspek, R., et al. 2021, *PASP*, 133, 095002
- Feiden, G. A. 2016, *A&A*, 593, A99
- Ferreira, J. M. 2000, *MNRAS*, 316, 647
- Gagné, J., Mamajek, E. E., Malo, L., et al. 2018, *ApJ*, 856, 23
- Gaia Collaboration, Brown, A. G. A., Vallenari, A., et al. 2018, *A&A*, 616, A1
- Gaia Collaboration, Smart, R. L., Sarro, L. M., et al. 2021, *A&A*, 649, A6
- Gaia Collaboration, Vallenari, A., Brown, A. G. A., et al. 2022, *arXiv e-prints*, arXiv:2208.00211
- Gaidos, E., Mann, A. W., Rojas-Ayala, B., et al. 2022, *MNRAS*, 514, 1386
- Gilbert, E. A., Barclay, T., Quintana, E. V., et al. 2022, *AJ*, 163, 147
- Gray, D. F. 1992, The observation and analysis of stellar photospheres., Vol. 20
- Gully-Santiago, M. A., Herczeg, G. J., Czekala, I., et al. 2017, *ApJ*, 836, 200
- Günther, M. N., Berardo, D. A., Ducrot, E., et al. 2022, *AJ*, 163, 144
- Hallinan, G., Littlefair, S. P., Cotter, G., et al. 2015, *Nature*, 523, 568
- Harris, C. R., Millman, K. J., van der Walt, S. J., et al. 2020, *Nature*, 585, 357
- Hartmann, L., Herczeg, G., & Calvet, N. 2016, *ARA&A*, 54, 135
- Henden, A. A., Templeton, M., Terrell, D., et al. 2016, VizieR Online Data Catalog, II/336
- Hesser, J. E., Ugarte, P. P., & Moreno, H. 1977, *ApJL*, 216, L31
- Hippke, M., David, T. J., Mulders, G. D., & Heller, R. 2019, *arXiv:1906.00966 [astro-ph]*, arXiv: 1906.00966
- Hippke, M., David, T. J., Mulders, G. D., & Heller, R. 2019, *AJ*, 158, 143
- Howard, A. W., Johnson, J. A., Marcy, G. W., et al. 2010, *ApJ*, 721, 1467
- Howell, S. B., Sobeck, C., Haas, M., et al. 2014, *PASP*, 126, 398
- Izidoro, A., & Raymond, S. N. 2018, in *Handbook of Exoplanets*, ed. H. J. Deeg & J. A. Belmonte, 142

- Jardine, M., & Collier Cameron, A. 2019, *MNRAS*, **482**, 2853
- Jayaraman, R., Hubrig, S., Holdsworth, D. L., et al. 2022, *ApJL*, **924**, L10
- Jeffries, R. D. 1993, *MNRAS*, **262**, 369
- Jenkins, J. M., Twicken, J. D., McCauliff, S., et al. 2016, in Society of Photo-Optical Instrumentation Engineers (SPIE) Conference Series, Vol. 9913, Software and Cyberinfrastructure for Astronomy IV, ed. G. Chiozzi & J. C. Guzman, 99133E
- Johns-Krull, C. M., Prato, L., McLane, J. N., et al. 2016, *ApJ*, **830**, 15
- Justesen, A. B., & Albrecht, S. 2021, *ApJ*, **912**, 123
- Kenyon, S. J., & Hartmann, L. 1995, *ApJS*, **101**, 117
- Kerr, R. M. P., Rizzuto, A. C., Kraus, A. L., & Offner, S. S. R. 2021, *ApJ*, **917**, 23
- Kochukhov, O. 2021, *A&A Rv*, **29**, 1
- Kochukhov, O., Lundin, A., Romanyuk, I., & Kudryavtsev, D. 2011, *ApJ*, **726**, 24
- Koen, C. 2021, *MNRAS*, **500**, 1366
- . 2023, *MNRAS*, **518**, 2921
- Landstreet, J. D., & Borra, E. F. 1978, *ApJL*, **224**, L5
- Leitzinger, M., Odert, P., Zaqrashvili, T. V., et al. 2016, *MNRAS*, **463**, 965
- Li, R., Chen, Y.-X., & Lin, D. N. C. 2022, *MNRAS*, **510**, 5246
- Lichtenberg, T., Schaefer, L. K., Nakajima, M., & Fischer, R. A. 2022, arXiv e-prints, arXiv:2203.10023
- Lightkurve Collaboration, Cardoso, J. V. d. M., Hedges, C., et al. 2018, Lightkurve: Kepler and TESS time series analysis in Python, Astrophysics Source Code Library, record ascl:1812.013
- MacLeod, M., & Oklopčić, A. 2022, *ApJ*, **926**, 226
- McCann, J., Murray-Clay, R. A., Kratter, K., & Krumholz, M. R. 2019, *ApJ*, **873**, 89
- Mikulášek, Z., Krtička, J., Shultz, M. E., et al. 2020, in Stellar Magnetism: A Workshop in Honour of the Career and Contributions of John D. Landstreet, ed. G. Wade, E. Alecian, D. Bohlender, & A. Sigut, Vol. 11, 46
- Murphy, S. J., Lawson, W. A., & Bessell, M. S. 2013, *MNRAS*, **435**, 1325
- Nakajima, R. 1985, *Ap&SS*, **116**, 285
- Oksala, M. E., Wade, G. A., Townsend, R. H. D., et al. 2012, *MNRAS*, **419**, 959
- Onitsuka, M., Fukui, A., Narita, N., et al. 2017, *PASJ*, **69**, L2
- Paegert, M., Stassun, K. G., Collins, K. A., et al. 2021, arXiv e-prints, arXiv:2108.04778
- Palumbo, E. K., Montet, B. T., Feinstein, A. D., et al. 2022, *ApJ*, **925**, 75
- Park, R. S., Vaughan, A. T., Konopliv, A. S., et al. 2019, *Icarus*, **319**, 812
- Pass, E. K., Charbonneau, D., Irwin, J. M., & Winters, J. G. 2022, *ApJ*, **936**, 109
- Pecaut, M. J., & Mamajek, E. E. 2016, *MNRAS*, **461**, 794
- Penoyre, Z., Belokurov, V., & Evans, N. W. 2022, *MNRAS*, **513**, 5270
- Pérez Paolino, F., Bary, J. S., Petersen, M. S., et al. 2023, *ApJ*, **946**, 10
- Petit, V., Owocki, S. P., Wade, G. A., et al. 2013, *MNRAS*, **429**, 398
- Popinchalk, M., Faherty, J. K., Curtis, J. L., et al. 2023, *ApJ*, **945**, 114
- Pribulla, T., Borkovits, T., Jayaraman, R., et al. 2023, *MNRAS*, **524**, 4220
- Rajpurohit, A. S., Reylé, C., Allard, F., et al. 2013, *A&A*, **556**, A15
- Rappaport, S., Barclay, T., DeVore, J., et al. 2014, *ApJ*, **784**, 40
- Rappaport, S., Levine, A., Chiang, E., et al. 2012, *ApJ*, **752**, 1
- Rappaport, S., Vanderburg, A., Jacobs, T., et al. 2018, *MNRAS*, **474**, 1453
- Rateznböck, S., Meingast, S., Alves, J., Möller, T., & Bomze, I. 2020, *A&A*, **639**, A64
- Rebull, L. M., Stauffer, J. R., Cody, A. M., et al. 2018, *AJ*, **155**, 196
- Rebull, L. M., Stauffer, J. R., Hillenbrand, L. A., et al. 2022, *AJ*, **164**, 80
- Rebull, L. M., Stauffer, J. R., Bouvier, J., et al. 2016, *AJ*, **152**, 114
- Reinhold, T., Bell, K. J., Kuszlewicz, J., Hekker, S., & Shapiro, A. I. 2019, *A&A*, **621**, A21
- Ricker, G. R., Winn, J. N., Vanderspek, R., et al. 2015, *Journal of Astronomical Telescopes, Instruments, and Systems*, **1**, 014003
- Rivinius, T., Carciofi, A. C., & Martayan, C. 2013, *A&A Rv*, **21**, 69
- Rizzuto, A. C., Newton, E. R., Mann, A. W., et al. 2020, *AJ*, **160**, 33
- Robinson, C. E., Espaillat, C. C., & Owen, J. E. 2021, *ApJ*, **908**, 16
- Rodriguez, D. R., van der Plas, G., Kastner, J. H., et al. 2015, *A&A*, **582**, L5
- Sanchis-Ojeda, R., Rappaport, S., Pallè, E., et al. 2015, *ApJ*, **812**, 112
- Sanderson, H., Jardine, M., Collier Cameron, A., Morin, J., & Donati, J. F. 2023, *MNRAS*, **518**, 4734
- Saur, J., Neubauer, F. M., Connerney, J. E. P., Zarka, P., & Kivelson, M. G. 2004, in Jupiter. The Planet, Satellites and Magnetosphere, ed. F. Bagenal, T. E. Dowling, & W. B. McKinnon, Vol. 1, 537
- Servén, D., & Brummitt, C. 2018, pyGAM: Generalized Additive Models in Python
- Skrutskie, M. F., Cutri, R. M., Stiening, R., et al. 2006, *AJ*, **131**, 1163
- Somers, G., Cao, L., & Pinsonneault, M. H. 2020, *ApJ*, **891**, 29
- Speagle, J. S. 2020, *MNRAS*, **493**, 3132
- Stassun, K. G., Kratter, K. M., Scholz, A., & Dupuy, T. J. 2012, *ApJ*, **756**, 47
- Stassun, K. G., Oelkers, R. J., Paegert, M., et al. 2019, *AJ*, **158**, 138

- Stauffer, J., Collier Cameron, A., Jardine, M., et al. 2017, *AJ*, 153, 152
- Stauffer, J., Rebull, L., David, T. J., et al. 2018, *AJ*, 155, 63
- Stellingwerf, R. F. 1978, *ApJ*, 224, 953
- Townsend, R. H. D., & Owocki, S. P. 2005, *MNRAS*, 357, 251
- Townsend, R. H. D., Owocki, S. P., & Groote, D. 2005, *ApJL*, 630, L81
- Vanderburg, A., Johnson, J. A., Rappaport, S., et al. 2015, *Nature*, 526, 546
- Vial, J.-C., & Engvold, O. 2015, *Astrophysics and Space Science Library*, Vol. 415, Solar Prominences
- Vines, J. I., & Jenkins, J. S. 2022, *MNRAS*, 513, 2719
- Virtanen, P., Gommers, R., Oliphant, T. E., et al. 2020, *Nature Methods*, 17, 261
- Vogt, S. S., Allen, S. L., Bigelow, B. C., et al. 1994, in *Society of Photo-Optical Instrumentation Engineers (SPIE) Conference Series*, Vol. 2198, *Instrumentation in Astronomy VIII*, ed. D. L. Crawford & E. R. Craine, 362
- Vos, J. M., Faherty, J. K., Gagné, J., et al. 2022, *ApJ*, 924, 68
- Waugh, R. F. P., & Jardine, M. M. 2022, *MNRAS*, 514, 5465
- Winters, J. G., Charbonneau, D., Henry, T. J., et al. 2021, *AJ*, 161, 63
- Winters, J. G., Henry, T. J., Jao, W.-C., et al. 2019, *AJ*, 157, 216
- Wright, E. L., Eisenhardt, P. R. M., Mainzer, A. K., et al. 2010, *AJ*, 140, 1868
- York, D. G., Adelman, J., Anderson, John E., J., et al. 2000, *AJ*, 120, 1579
- Zhan, Z., Günther, M. N., Rappaport, S., et al. 2019, *ApJ*, 876, 127
- Zieba, S., Zwintz, K., Kenworthy, M. A., & Kennedy, G. M. 2019, *A&A*, 625, L13
- Zuckerman, B. 2019, *ApJ*, 870, 27
- Zuckerman, B., Bessell, M. S., Song, I., & Kim, S. 2006, *ApJL*, 649, L115

Table 1. Bona fide, candidate, and debunked complex rotators from the TESS 2-minute data. For internal review, full versions are available here <https://www.dropbox.com/scl/fo/twn4s9ckbevf75jqhtoy1/h?rlkey=t5cn8cx2uoc2ptdm9e570kp1b&dl=0>

TIC –	<i>T</i> mag	<i>d</i> pc	$G_{\text{BP}} - G_{\text{RP}}$ mag	RUWE –	<i>P</i> hr	Assoc	Age Myr	T_{eff} K	R_* R_{\odot}	M_* M_{\odot}	R_{cr} R_*	P_{sec} hr	Quality –	Bin –	N_{sector} –
368129164	9.29	18.3	2.89	6.95	6.44	ABDMG	149	3140	0.71	0.4	1.81	2.60	1	011	3
405754448	9.63	92.6	1.75	6.81	12.92	LCC	15	4273	1.5	0.82	1.74	134.4	1	011	5
167664935	10.31	62.5	2.52	5.05	14.05	UCL	16	3325	1.42	0.38	1.5	10.71	1	011	3
311092148	11.03	26.8	3.03	1.5	7.86	COL	42	3035	0.5	0.27	2.6	–	1	000	1
402980664	11.11	21.3	3.04	1.48	18.56	COL	42	3080	0.37	0.22	5.76	–	1	000	10
50745567	11.28	38.0	3.22	3.95	6.34	BPMG	24	3014	0.67	0.28	1.68	28.55	1	011	2
59836633	11.38	61.9	2.71	1.21	14.96	BPMG	24	3282	0.82	0.48	2.91	–	1	000	3
425933644	11.4	43.2	2.82	10.29	11.67	THA	45	3151	0.63	0.4	3.06	–	1	010	6
142173958	11.61	70.6	3.09	2.9	11.76	TWA	10	3028	1.15	0.26	1.45	12.84	1	011	3
146539195	11.62	48.2	3.37	2.86	6.73	BPMG	24	2898	0.8	0.24	1.38	7.29	1	011	2
206544316	11.63	42.8	2.89	1.26	7.73	THA	45	3114	0.57	0.35	2.44	–	1	000	6
335598085	11.9	105.5	2.85	2.79	15.85	LCC	15	3119	1.34	0.28	1.56	17.94	1	011	3
405910546	12.11	111.9	2.36	1.09	37.99	LCC	15	3455	0.92	0.6	5.26	–	1	100	4
272248916	12.15	80.5	2.83	5.5	8.9	UCL	16	3193	0.81	0.4	1.97	50.7	1	011	3
178155030	12.17	46.8	2.91	1.29	11.67	THA	45	3097	0.49	0.3	3.53	–	1	000	4
224283342	12.29	38.0	3.04	1.27	21.3	COL	42	3050	0.39	0.22	6.08	–	1	100	3
89026133	12.31	131.6	2.82	4.0	11.2	UCL	16	3188	1.33	0.31	1.29	27.83	1	011	3
234295610	12.51	48.1	3.04	1.13	18.29	THA	45	3074	0.44	0.27	5.09	–	1	000	3
118449916	12.54	97.1	3.09	25.18	12.31	TAU	2	3025	1.04	0.28	1.7	6.71	1	011	4
67897871	12.55	148.2	3.01	2.55	6.23	USCO	10	3082	1.5	0.18	0.65	6.72	1	011	2
353730181	12.65	106.6	2.75	1.23	13.51	TAU	2	3253	0.8	0.41	2.65	–	1	000	4
201898222	12.68	42.2	3.21	1.29	10.7	THA	45	2996	0.39	0.2	3.69	13.62	1	001	5
264767454	12.73	123.3	2.93	12.3	10.01	COL(?)	42	3150	1.0	0.42	1.76	20.62	1	011	13
442571495	12.75	80.8	3.03	1.64	9.59	UCL	16	3099	0.65	0.3	2.35	13.82	1	001	3
2234692	12.8	53.7	3.0	1.2	6.52	COL	42	3098	0.44	0.26	2.56	59.8	1	001	7
94088626	12.88	57.6	3.07	1.12	6.6	ARG	45	3090	0.46	0.27	2.53	–	1	000	2
264599508	12.88	79.7	3.01	1.89	7.9	COL	42	3098	0.62	0.4	2.4	8.99	1	001	7
363963079	12.92	83.1	3.09	8.0	7.82	ARG	45	3040	0.67	0.4	2.21	7.41	1	011	7
193831684	13.03	51.6	3.23	1.16	31.02	BPMG	24	2971	0.42	0.2	6.87	–	1	000	3
177309964	13.1	91.0	2.94	1.15	10.88	CAR	45	3125	0.62	0.4	2.95	–	1	000	34
425937691	13.18	43.1	3.77	2.86	4.82	THA	45	2782	0.41	0.16	1.91	3.22	1	011	5
141146667	13.28	57.6	3.28	1.23	3.93	FIELD	NaN	2968	0.42	NaN	NaN	–	1	000	6
332517282	13.29	39.0	3.27	1.05	9.67	ABDMG	149	2975	0.28	0.2	4.87	–	1	000	3
144486786	13.3	77.4	3.05	15.05	6.82	COL	42	3074	0.51	0.3	2.38	11.49	1	011	4
38820496	13.3	44.1	3.37	1.08	15.73	THA	45	2903	0.34	0.16	5.13	–	1	000	5
289840926	13.31	40.2	3.75	1.16	4.8	BPMG	24	2807	0.36	0.14	2.05	15.64	1	001	3
404144841	13.33	77.1	3.19	1.11	10.74	TWA	10	3008	0.52	0.22	2.86	–	1	000	4
89463560	13.45	123.9	2.97	1.31	9.43	ARG	45	3055	0.75	0.37	2.15	7.76	1	001	10
300651846	13.49	109.2	2.86	1.16	8.26	CAR	45	3136	0.62	0.4	2.44	–	1	000	31
267953787	13.49	130.5	3.59	1.2	17.46	TAU	2	2826	1.06	0.12	1.59	–	1	000	4
68812630	13.6	123.8	3.22	1.63	9.04	TAU	2	2996	0.76	0.27	1.86	5.28	1	001	3
141306513	13.65	50.2	3.4	1.08	13.36	THA	45	2964	0.32	0.16	4.85	–	1	000	2
201789285	14.03	45.4	3.82	1.19	3.64	THA	45	2757	0.3	0.12	2.02	–	1	000	5
294328887	14.23	97.1	3.22	1.05	8.51	CARN	200	2994	0.45	0.35	3.33	–	1	000	35

Table 1 *continued*

Table 1 (*continued*)

312410638	14.3	136.9	3.12	1.09	28.06	UCL	16	3030	0.58	0.25	5.11	-	1	000	3
38539720	14.52	129.4	3.37	1.2	9.16	PERI	120	2924	0.57	0.25	2.43	-	1	000	1
359892714	14.53	95.5	4.04	1.07	11.33	EPSC	3	2675	0.55	0.13	2.36	-	1	000	6
118769116	14.58	119.0	3.6	1.13	8.56	TAU	2	2852	0.56	0.2	2.18	-	1	000	4
440725886	14.69	135.1	2.96	1.06	3.92	PLE	112	3109	0.45	0.35	1.99	-	1	000	5
397791443	15.01	151.1	3.1	1.06	6.95	IC2602	46	3031	0.48	0.26	2.46	-	1	000	6
160329609	9.65	8.7	3.4	1.18	24.31	ARG	45	2912	0.35	0.16	6.6	-	0	000	3
148646689	12.14	140.4	2.44	1.7	10.63	UCL	16	3466	1.25	0.55	1.61	13.37	0	001	3
280945693	12.27	98.2	2.97	1.16	15.27	LCC	15	3103	1.09	0.31	1.94	-	0	100	5
165184400	12.37	43.2	3.02	1.24	15.91	THA	45	3076	0.42	0.25	4.74	-	0	000	4
245834739	12.55	115.4	2.85	1.49	10.47	TAU	2	3112	1.02	0.36	1.68	9.86	0	001	6
125843782	13.01	127.7	2.86	1.21	44.17	TAU	2	3135	0.9	0.35	4.97	-	0	000	4
244161191	13.17	44.7	3.54	1.28	7.17	COL	42	2860	0.38	0.18	2.8	8.39	0	001	3
231058925	13.17	51.2	3.25	1.35	8.87	THA	45	2978	0.38	0.2	3.33	-	0	000	5
301676454	13.4	70.7	3.07	1.24	9.18	ARG	45	3009	0.47	0.25	2.96	-	0	000	1
58084670	13.58	140.2	2.82	1.06	11.16	FIELD	NaN	3138	0.77	NaN	NaN	-	0	000	6
67745212	13.63	27.8	3.8	1.11	5.12	COL	42	2781	0.21	0.09	3.17	-	0	000	2
5714469	13.73	78.3	3.65	1.12	10.35	UCL	16	2828	0.54	0.18	2.53	-	0	000	3
259586708	13.82	95.6	2.93	1.17	22.52	COL	42	3133	0.46	0.29	5.84	-	0	000	7
435903839	11.95	80.7	2.49	17.7	10.82	ABDMG(?)	149	3458	0.76	0.54	2.66	-	-1	010	6
57830249	11.96	48.8	3.2	1.34	43.82	TWA	10	2948	0.7	0.25	5.63	-	-1	000	3
193136669	13.06	61.1	3.49	1.22	37.64	TWA	10	2855	0.58	0.19	5.62	-	-1	000	4

NOTE—This table includes 50 CRs (Quality flag 1), 13 ambiguous CRs (Quality flag 0), and 3 impostors (Quality flag -1). The three-bit binarity flag “Bin” is for Gaia DR3 `radial_velocity_error` outliers (bit 1), Gaia DR3 `ruwe` outliers (bit 2), and stars with multiple TESS periods (bit 3). The machine-readable version, available online, includes additional columns for the Gaia DR2 and DR3 source identifiers, as well as the stellar parameter uncertainties. The age uncertainties are typically $\approx \pm 10\%$, but can be asymmetric. The median statistical uncertainties on the temperature, radius, and mass are $\pm 50\text{ K}$, $\pm 4\%$ and $\pm 9\%$ respectively. N_{sector} denotes the number of TESS sectors for which *any* data are expected to be acquired between July 2018 and Oct 2024. This number is generally greater than the number of sectors for which 120-second cadence data exist. Association names and provenance follow conventions adopted by Gagné et al. (2018): ABDMG: AB Doradus moving group (Bell et al. 2015). ARG: Argus (Zuckerman 2019). BPMG: β Pic moving group (Bell et al. 2015). CARN: Carina Near moving group (Zuckerman et al. 2006). COL: Columba (Bell et al. 2015). EPSC: ϵ Chamæleonis (Murphy et al. 2013). LCC: Lower Centaurus Crux (Pecaut & Mamajek 2016). PERI: Pisces-Eridani (Curtis et al. 2019). PLE: Pleiades (Dahm 2015). TAU: Taurus (Kenyon & Hartmann 1995). THA: Tucana-Horologium association (Bell et al. 2015). TWA: TW Hydriæ association (Bell et al. 2015). UCL: Upper Centaurus Lupus (Pecaut & Mamajek 2016). USCO: Upper Scorpius (Pecaut & Mamajek 2016). The “(?)” string denotes low-confidence membership.

APPENDIX

A. THE RING HYPOTHESIS

One hypothesis for the CRs, presented by Zhan et al. (2019), is that the star might be “*orbited by one or more rings composed of dust-size or somewhat larger particles... The ring particles would move in Keplerian orbits at relatively large distances from the star, and therefore the sublimation lifetime would not be an issue even if the particles are dust-like in size.*” A sketch of this scenario was presented by Zhan et al. (2019), in their Figure 11. An example set of proposed parameters involved a ring inclined with respect to the stellar spin axis by a few degrees, and with inner and outer radii of 10 and 15 stellar radii.

One concern with the ring hypothesis is that if a cool spot were to transit behind the ring, it would produce a brightening, not a dimming. Most CRs show dimmings. The ring scenario would therefore imply that large hot spots are common in the photospheres of pre-main-sequence M dwarfs. Empirical evidence however suggests that cool spots dominate the the optical variability of disk-free pre-main-sequence stars. This evidence includes flux excursions caused by spot-crossings during planetary transits (e.g. Rizzuto et al. 2020; Gilbert et al. 2022), correlations between simultaneous photometric and chromospheric time-series (Reinhold et al. 2019), and stellar spectra that show molecules that only form at cool temperatures (e.g. Gully-Santiago et al. 2017; Pérez Paolino et al. 2023).

An independent concern with the ring hypothesis is that it is fine-tuned. The model requires specific locations for the inner edge and the outer edge of the ring, an inclination that yields a band with a specific apparent size, and material in the ring that must be optically thick while also being homogeneous enough to not induce any apparent photometric variability. It is challenging

to ascribe specific probabilities to any one of these factors. However the requirement that they all be simultaneously met seems sufficiently severe to disfavor this scenario.

B. TIC 300651846

Figures 11 and 12 show 120-second cadence data for TIC 300651846, a CR in the TESS continuous viewing zone. If it were not for the existence of TIC 402980664, this source would probably have received greater attention. With the exception of a few sectors, TESS data will exist for TIC 300651846 for at least Sectors 1-12, 27-39, and 61-69. While most of the available data exist in the full frame images, Figures 11 and 12 focus only on the currently available 120-second cadence data.

During Sectors 32-39, the source shows between one and four local minima per cycle. During the early portions of Sectors 61-65, it is somewhat more complex, with at least five clear local minima per cycle. As the source evolves, this complexity decreases, while the sharpness of one of the minima appears to increase. We did not find evidence for any obvious “state-switches” analogous to those that we observed in LP 12-502; gradual evolution over timescales of \approx 50-100 cycles seem to be the norm for TIC 300651846. Unlike the TIC 402980664 river plots (Figure 9), we did not subtract any “continuum sinusoid” for this source, because the continuum is not as obviously defined.

C. NO SIGNIFICANT POWER AT 20 SECOND CADENCE

TESS was the first instrument to show that CR light curves contain power at timescales of a few minutes (Zhan et al. 2019; Günther et al. 2022). This advance was enabled by the fifteen-fold faster cadence in the TESS 2-minute data, relative to K2. A logical follow-up is to ask whether the periodic components of the CR light curves contain power at timescales below one minute. Between 2020 and 2021, we observed 10 CRs at 20-second cadence with TESS in order to explore this question (TESS DDT029). The stars were TICs 142173958, 146539195, 24518895, 276453848, 264599508, 363963079, 144486786, 408188366, 300651846, 262400835. These sources were selected from CRs known at the time to have short periods and sharp features when observed at 2-minute cadence. Comparing the 20-second to 120-second data for these stars (data available on MAST), we concluded that these CRs did not contain appreciable power at timescales shorter than a few minutes.

D. THE CRS ARE NOT OBVIOUSLY ACCRETING

We acquired iodine-free reconnaissance spectra using Keck/HIRES for three CRs. The goals were to determine the chromospheric activity levels, and to check for indications of either accretion or spectroscopic binarity. We acquired a 15 minute exposure of TIC 146539195 on 2023 January 3, a 15 minute exposure of TIC 264599508 on 2023 January 9, and a 30 minute exposure of TIC 402980664 on 2023 July 10. The acquisition and analysis followed the usual techniques of the California Planet Survey (Howard et al. 2010). Figure 13 shows cutouts from the resulting spectra, centered on the Ca II HK windows, H α , and the Li I 6708 Å doublet. The Ca II H emission line is blended with He. While a more detailed analysis will be left for future work, these spectra confirm previous understanding established by Stauffer et al. (2017) that the stars are chromospherically active M dwarfs in the “weak-lined” T Tauri regime (e.g. Briceño et al. 2019, Figure 15). Their H α equivalent widths, at \approx 14 Å, \approx 3 Å, and \approx 8 Å (for TIC 264599508, 146539195, and 402980664 respectively) are consistent with purely chromospheric emission. The blue excess in TIC 264599508 could be explained by a second unresolved star; the TESS light curve for this source shows both the 7.90 hr CR signal, and a 9.00 hr rotation signal with comparable amplitude.

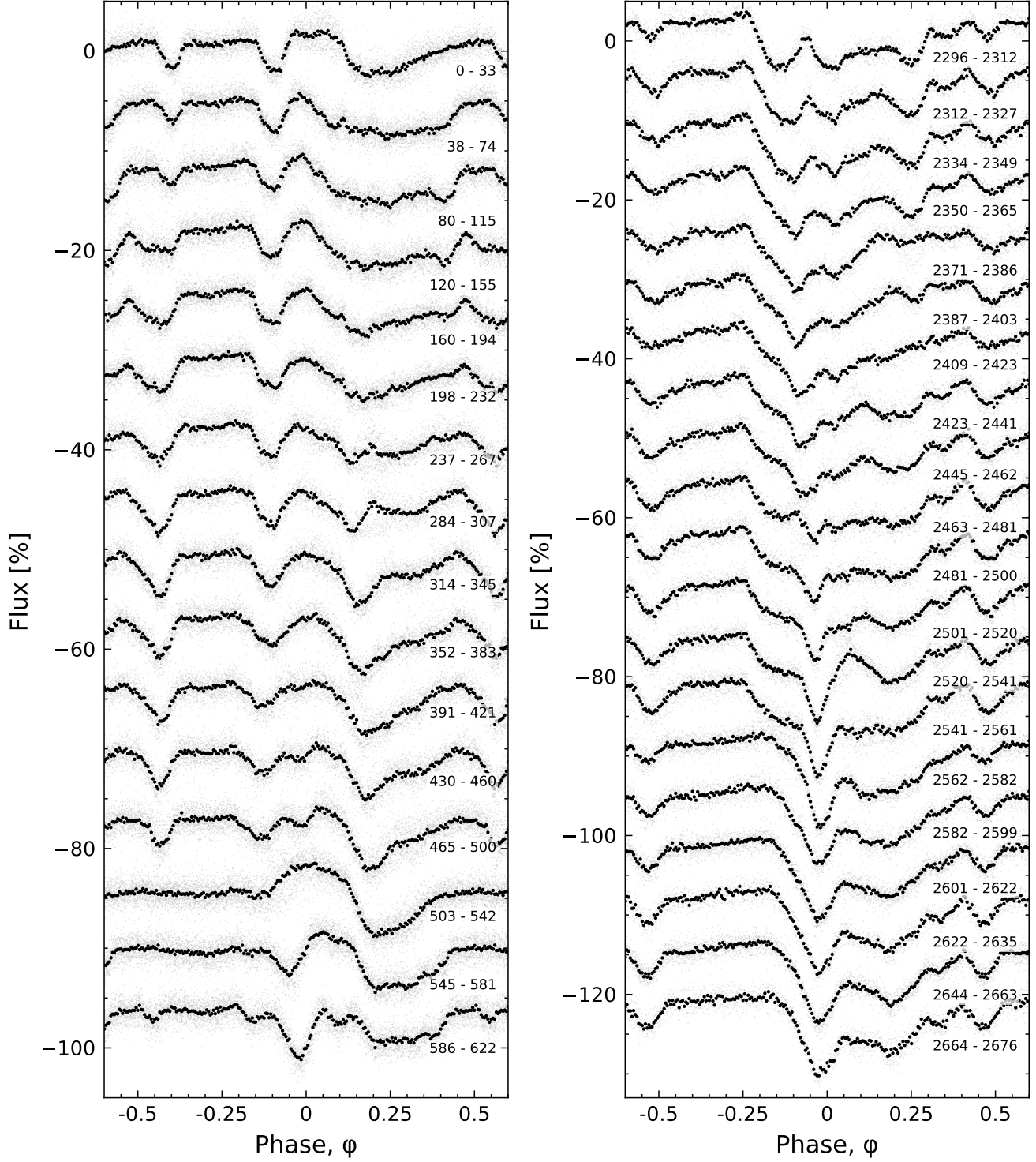


Figure 11. Light curve evolution of TIC 300651846. All available 120-second cadence data as of 2023 Aug 11 are shown. Cycles 0 to 622 span TESS Sectors 32-39 (Nov 2020–June 2021); cycles 2296-2676 span Sectors 61-65 (Jan–June 2023). We assumed a 8.254 hr period and a fixed reference epoch (BTJD 2174.127) for both panels. Light curve segments are split based on the presence of gaps longer than three hours. Cycle numbers are listed in the lower-right of each light curve segment.

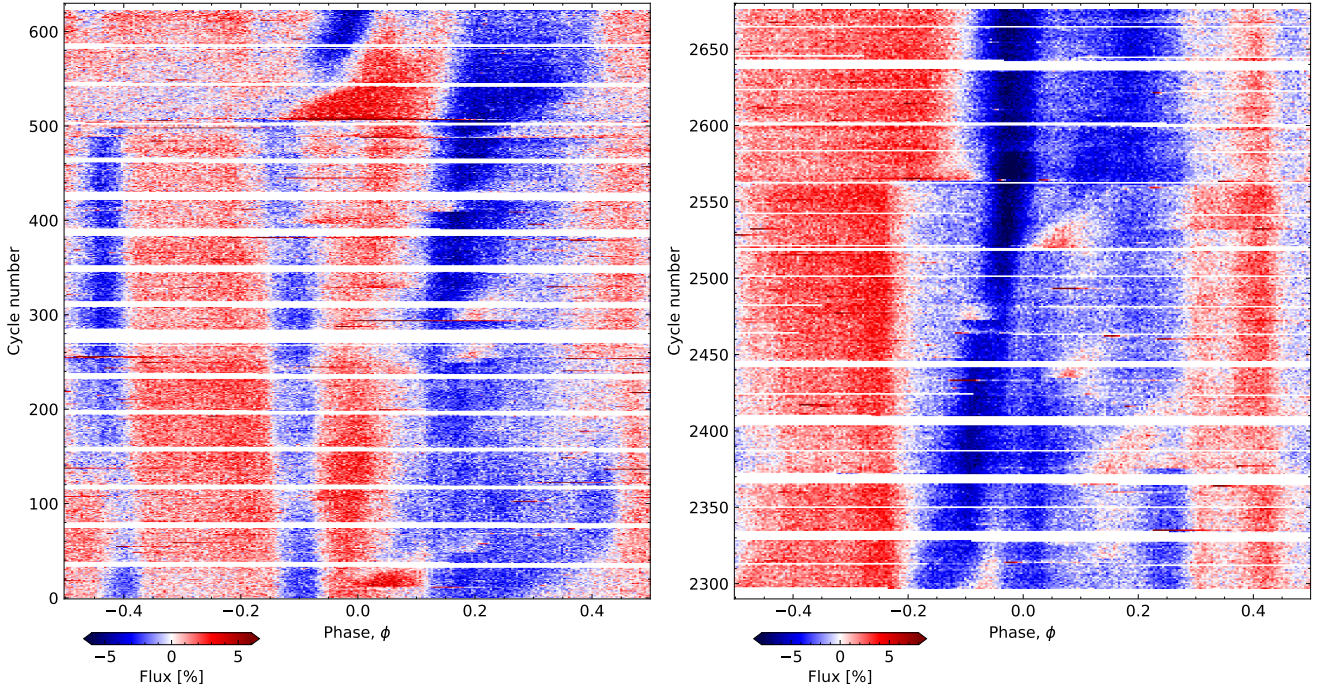


Figure 12. River plots of TIC 300651846. This is an alternative visualization of the data in Figure 11. All available 120-second cadence data as of 2023 Aug 11 are shown. Cycles 0 to 622 span TESS Sectors 32-39 (Nov 2020–June 2021); cycles 2296-2676 span Sectors 61-65 (Jan–June 2023). We assumed $P=8.254$ hr and $t_0=2174.127$ [BTJD]. Note that the two panels have slightly different color scales.

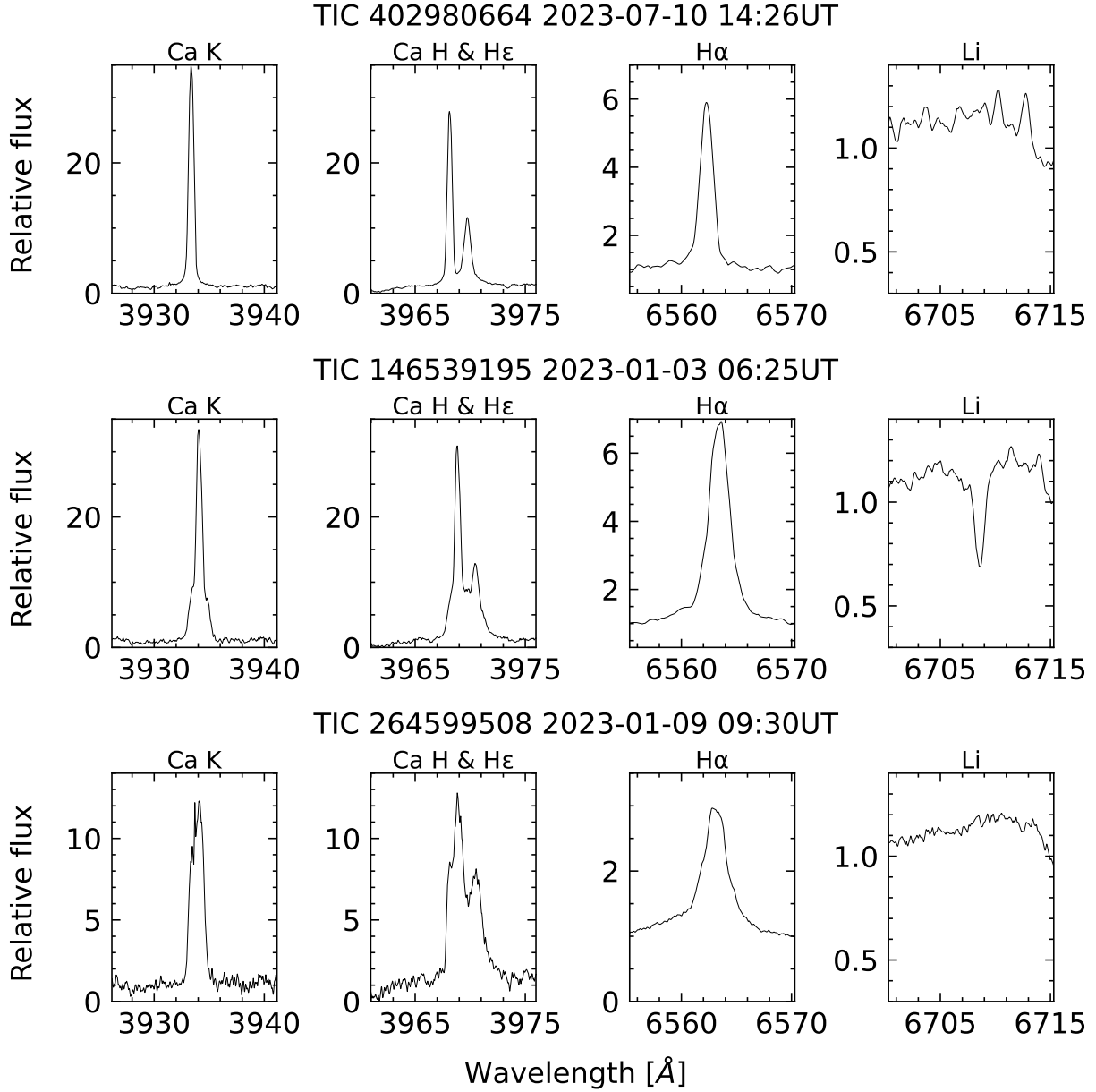


Figure 13. Spectral age and activity diagnostics for three CRs. Wavelengths are in air; the continuum normalization is relative to the entire order. The H α emission strength classifies the stars as weak-lined T Tauris. The lithium detection for TIC 146539195 is consistent with its mass and β Pic membership; the non-detections for TIC 402980664 and TIC 264599508 are consistent with the ≈ 42 Myr age implied by their membership in the Columba moving group.